

# Interfacial Control of Orbital Occupancy and Spin State in $\text{LaCoO}_3$

Ellen M. Kiens,<sup>1, a)</sup> Nicolas Gauquelin,<sup>2</sup> Arno Annys,<sup>2</sup> Emma van der Minne,<sup>1</sup> Iris C.G. van den Bosch,<sup>1</sup> Matthijs A. van Spronsen,<sup>3</sup> Zezhong Zhang,<sup>2</sup> Annick de Backer,<sup>2</sup> Sandra van Aert,<sup>2</sup> Jo Verbeeck,<sup>2</sup> Gertjan Koster,<sup>1</sup> Bastian Mei,<sup>1, 4</sup> Frank M.F. de Groot,<sup>5</sup> and Christoph Baeumer<sup>1, 6, b)</sup>

<sup>1)</sup>MESA+ Institute for Nanotechnology, Faculty of Science and Technology, University of Twente, 7500 AE Enschede, The Netherlands

<sup>2)</sup>Electron Microscopy for Materials Science, University of Antwerp, Campus Groenenborger, Groenenborgerlaan 171, 2020 Antwerpen, Belgium

<sup>3)</sup>Diamond Light Source, Harwell Science and Innovation Campus, Didcot, Oxfordshire OX11 0DE, United Kingdom

<sup>4)</sup>Laboratory of Industrial Chemistry, Ruhr University Bochum, 44780 Bochum, Germany

<sup>5)</sup>Materials Chemistry and Catalysis, Debye Institute for Nanomaterials Science, Utrecht University, Universiteitsweg 99, 3584 CG Utrecht, The Netherlands

<sup>6)</sup>Peter Gruenberg Institute 7, Forschungszentrum Juelich GmbH, 52428 Juelich, Germany

(Dated: 4 December 2025)

Transition metal oxides exhibit a wide range of tunable electronic properties arising from the complex interplay of charge, spin, and lattice degrees of freedom, governed by their  $d$  orbital configurations, making them particularly interesting for oxide electronics and (electro)catalysis. Perovskite oxide heterointerfaces offer a promising route to engineer these orbital states. In this work, we tune the Co  $3d$  orbital occupancy in  $\text{LaCoO}_3$  from a partial  $d^7$  to a partial  $d^5$  state through interfacial engineering with  $\text{LaTiO}_3$ ,  $\text{LaMnO}_3$ ,  $\text{LaAlO}_3$  and  $\text{LaNiO}_3$ . Using X-ray absorption spectroscopy combined with charge transfer multiplet calculations, we identify differences in the Co valence and spin state for the series of oxide heterostructures.  $\text{LaTiO}_3$  and  $\text{LaMnO}_3$  interfaces result in interfacial charge transfer towards  $\text{LaCoO}_3$ , resulting in a partial  $d^7$  orbital occupancy, while a  $\text{LaNiO}_3$  interface results in a partial Co  $d^5$  occupancy. Strikingly, a  $\text{LaAlO}_3$  spacer layer between  $\text{LaNiO}_3$  and  $\text{LaCoO}_3$  results in a Co  $d^6$  low spin state. These results indicate that the Co spin state, like the valence state, is governed by the interfacial environment. High-resolution scanning transmission electron microscopy imaging reveals a clear connection between strain and spin configuration, emphasizing the importance of structural control at oxide interfaces. Overall, this work demonstrates that interfacial engineering simultaneously governs orbital occupancy and spin state in correlated oxides, advancing spin-engineering strategies in correlated oxides and offering new insights for the rational design of functional oxide heterostructures.

## I. INTRODUCTION

Transition metal oxides are of great technological importance due to their wide range of tunable electronic properties. The ordering and occupation of the outer  $d$  orbitals in these materials results in their structural, electronic, magnetic, optical and thermal properties. Moreover, the strongly correlated  $d$  electrons in these materials entangle charge, spin and structural degrees of freedom, giving rise to a variety of exotic phenomena such as magnetic ordering, metal-to-insulator transitions, multiferroics and superconductivity<sup>1,2</sup>. Engineering of the orbital configuration in these highly correlated materials can lead to new emerging physical properties.

Perovskite oxide heterointerfaces offer a platform to tune orbital configurations and thereby explore new electronic phenomena<sup>3,4</sup>. For example, by structural engineering, exploiting strain and oxygen octahedral coupling across the interface, electronic and magnetic properties can be tuned<sup>5–14</sup>. Additionally, when the materials on both sides of the interface have different electron chemical potential, charge transfer can take place. For epitaxial isopolar heterointerfaces, the oxygen octahedra form a continuous backbone throughout the heterostructure. This should cause the O  $2p$  levels of both

materials across the interface to align. To align the chemical potential of both materials, charge transfer across the interface is expected<sup>15</sup>. This picture differs from the extensively studied polar interface, where a polar overlayer and/or the creation of point defects give rise to different electronic states at the interface<sup>16</sup>.

Interfacial charge transfer across isopolar interfaces presents an alternative method to control the  $d$  orbital occupation to chemical doping. For example, divalent Co, Fe and Ni have been observed at the interface between  $\text{LaCoO}_3$ ,  $\text{LaFeO}_3$  and  $\text{LaNiO}_3$  with  $\text{LaTiO}_3$ <sup>11,17,18</sup>. Following the band alignment picture, the oxidation state of Co, Fe and Ni at these interfaces were attributed to interfacial electron transfer from Ti to the heavier transition metals. However, the experimental study of  $\text{LaTiO}_3$  interfaces is complex due to the propensity of  $\text{LaTiO}_3$  to overoxidize<sup>19,20</sup>.

Tuning the  $d$  orbital occupation of Co in  $\text{LaCoO}_3$  is of particular interest for two reasons. First, the intriguing spin state of  $\text{LaCoO}_3$  and its related ferromagnetic order has been extensively discussed in literature<sup>21–31</sup>. The ground state of Co in  $\text{LaCoO}_3$  is  $d^6$  and its spin state is dictated by the competition between the crystal field splitting energy between the  $3d$  orbitals into  $e_g$  and  $t_{2g}$  levels and the exchange energy. Bulk  $\text{LaCoO}_3$  exhibits a low spin state at low temperature (20 K) and an inhomogeneous mixed spin state at room temperature<sup>27</sup>. However, for thin films the spin state differs from the bulk single crystal due to epitaxial strain<sup>28–31</sup> and re-

<sup>a)</sup>Electronic mail: e.m.kiens@utwente.nl

<sup>b)</sup>Electronic mail: c.baeumer@utwente.nl

duced dimensionality<sup>32</sup>.

Second, Co based transition metal oxides are promising materials for (electro)catalysis. The  $d$  orbital occupation of perovskites has been identified as a descriptor of their performance in catalyzing the oxygen evolution reaction, which is the limiting half-reaction in electrochemical water splitting<sup>33</sup>.  $\text{LaCoO}_3$  is a promising electrocatalyst, for which control over the  $d$  orbital occupation might allow for tuning of its (electro)chemical reactivity. Lowering its  $d$  orbital occupation to a (partial)  $d^5$  ground state could result in a highly active electrocatalyst<sup>34,35</sup>. Although interfacial charge transfer at  $\text{LaCoO}_3$ -based interfaces has been reported previously<sup>17</sup>, a systematic investigation of charge transfer in both directions, as well as the connection between orbital occupancy and structural effects across different interfaces remains absent.

In this work, we aim to tune the  $d$  orbital occupation of Co in  $\text{LaCoO}_3$  by interfacial engineering from a partial  $d^5$  to a partial  $d^7$  state by fabrication of the interfaces shown in Figure 1. Following the band alignment picture proposed by Zhong and Hansmann<sup>15</sup>, a partial  $d^7$  occupation is expected at the interface with  $\text{LaTiO}_3$  and  $\text{LaMnO}_3$  while a partial  $d^5$  occupation is expected at the interface with  $\text{LaNiO}_3$ . Furthermore, we investigate blocking of charge transfer for the latter using a  $\text{LaAlO}_3$  spacer layer. We studied the Co electronic state by X-ray absorption spectroscopy (XAS). The relative contributions of different valence and spin states are attributed with the help of charge transfer multiplet (CTM) calculations. Next, we examined the intermixing effects and strain in the  $\text{LaCoO}_3$  layer for the different interfaces with scanning transmission electron microscopy (STEM). We find that Co valence and spin state are influenced by interfacial engineering and provide evidence that structural effects and strain are governing the  $d$  orbital occupation at these oxide interfaces.

## II. METHODS

### A. Experimental

Fully strained epitaxial thin films were grown with unit cell thickness control using pulsed laser deposition (PLD) with in-situ reflective high-energy electron diffraction (RHEED). The depositions were performed in a vacuum chamber with a base pressure of  $5 \times 10^{-8}$  mbar, equipped with in-situ RHEED (Staib instruments) and a KrF excimer laser with a wavelength of 248 nm (Coherent). The deposition parameters (Table S1) were varied slightly per material to facilitate layer-by-layer growth and thereby unit cell thickness control. After growth, the multilayers were cooled down in deposition pressure with  $25^\circ\text{C}/\text{min}$ . Each epitaxial multilayer was grown on  $\text{TiO}_2$  terminated<sup>36</sup>  $\text{Nb:SrTiO}_3$  0.5 wt% substrates in the (001) orientation (CrysTec GmbH, Germany). A 25 u.c.  $\text{LaNiO}_3$  was grown on top of the substrate to separate the interface of interest from the polar interface with  $\text{SrTiO}_3$ , and to ensure similar rotation and/or tilting of oxygen octahedra between samples<sup>37</sup>. A relatively low growth temperature ( $450^\circ\text{C}$ ) is chosen for the  $\text{LaNiO}_3$  to obtain B-site termination of this

layer<sup>38</sup>. The thickness of the  $\text{LaCoO}_3$  layer was chosen to be 4 u.c., as interfacial charge transfer is expected to extend 2-3 u.c. from the interface as previously reported by Araiz-Kanoutas *et al.*<sup>17</sup>. The thickness of the  $\text{LaBO}_3$  ( $B = \text{Ti, Mn, Ni}$ ) layers below and on top of the  $\text{LaCoO}_3$  were chosen to be just above this limit and therefore 4 u.c. as well. A 5 u.c.  $\text{LaNiO}_3$  capping layer on all samples prevented beam damage during XAS measurements and air exposure effects.

X-ray diffraction was used to obtain structural information on the macroscopic scale. Diffractograms were obtained using a Bruker D8 Discover with a rotating anode source, Montel optics and a 2D Eiger2 R 500K detector. A two-bounce channel-cut germanium monochromator was used to obtain  $\text{Cu-K}\alpha$  radiation and a 1 mm collimator was used for a well-defined beam size.

The morphology of the multilayers was examined by atomic force microscopy (AFM) using a Veeco Dimension Icon AFM in tapping mode in air with a Tespa-V2 cantilever (Bruker, Netherlands) and a silicon tip with a nominal tip radius of 20 nm.

The  $d$  orbital occupation of the 3d transition metals in the multilayers was studied by X-ray absorption spectroscopy (XAS) of the transition metal  $L$  edges. These experiments were performed at the Versatile Soft X-ray (VerSoX) beamline B07-b at Diamond Light Source<sup>39</sup>. Spectra were collected in total electron yield at room temperature in vacuum ( $10^{-8}$  mbar). The incident angle of the photons was perpendicular to the sample surface. We took at least three spectra at different positions per sample. Furthermore, an hour of consecutive scans on the  $\text{LaNiO}_3$ - $\text{LaCoO}_3$  multilayer shows no change in spectral shape upon X-ray radiation for Co. The spectra presented in this work are single scans. As no spatial or time-dependent changes were observed, these scans are assumed to be representative of the whole sample. For all spectra, a linear background was subtracted well before the edge after which the spectra were normalized to the edge jump, thereby accounting for the number of holes in the 3d shell.

Focused ion beam lamellas for Scanning Transmission Electron Microscopy (STEM) were prepared in an Helios Nanolab 650 in a Kamrath and Weiss vacuum transfer box and transferred directly to a Gatan TEM vacuum transfer holder as described elsewhere<sup>17,40-42</sup>.

STEM using High Angle Annular Dark Field (HAADF) imaging was performed using a FEI Titan 80-300 microscope operated at 300 kV. Electron Energy Loss Spectroscopy (STEM-EELS) measurements were performed using a monochromatic beam with a 200 meV energy resolution and an acceleration voltage of 120 kV on a FEI Titan 80-300 microscope. The Ti  $L$ , Co  $L$ , Mn  $L$ , Ni  $L$  edge, O  $K$  and La  $M$  edges were acquired in several measurements. The acquisition parameters were 0.2 s/pixel, 0.12 Å/pixel and 0.05 eV/pixel in the dual EELS mode. Collection angles for HAADF imaging and EELS were 70-160 mrad and 47 mrad, respectively.

EELS analysis was performed using the pyEELSModel software<sup>43</sup>. The Co  $L$  edge, Ti  $L$  edge, Mn  $L$  edge and O  $K$  edge traces were computed using the background removal routine. The Ni  $L$  edge traces were calculated by model-based fitting because of the strong overlap with the La  $M$  edge. The



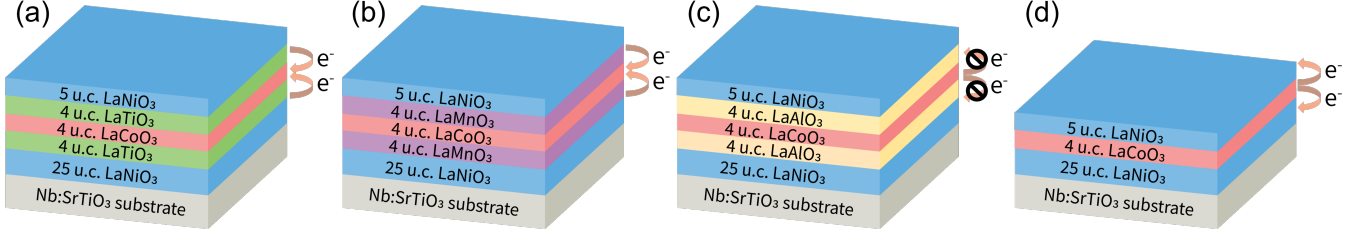


FIG. 1. Family of samples to study the four  $\text{LaBO}_3$ - $\text{LaCoO}_3$  interfaces, where  $B$  is (a) Ti, (b) Mn, (c) Al, (d) Ni.

model consisted of a constrained background component<sup>44</sup>, a La  $M$  reference edge extracted from a Ni-free region and a model Ni  $L$  edge using the theoretical cross-section from Z. Zhang *et al.*<sup>45</sup> combined with a generic fine structure component.

For Energy-dispersive X-ray spectroscopy (EDX) elemental mapping, multi-frame EDX data was acquired, using the simultaneously acquired HAADF signal. All frames were aligned using the SuperAlign routine<sup>46</sup>.

Strain maps were generated using the StatSTEM software<sup>47</sup>. In this approach, the images are modeled as a superposition of Gaussian functions centered on the atomic columns, allowing the positions of these columns to be determined with high accuracy and precision. The displacement field was obtained by comparing the measured atomic column positions with those of an ideal, undistorted reference lattice. The reference lattice is defined by the  $\text{SrTiO}_3$  substrate at the bottom of the structure. Specifically, the projected lattice vectors along the **a** and **b** directions are determined from the measured atomic column positions of  $\text{SrTiO}_3$ . These vectors are then used to construct a reference lattice, which serves as the basis for measuring strain throughout the entire layered structure. These displacement vectors were then projected onto the local lattice basis defined by the crystallographic directions **a** and **b**. For each analysis region, the deformation gradient tensor ( $F$ ) was calculated from the reference and deformed displacement fields. The Cauchy strain tensor ( $\epsilon$ ) was subsequently computed according to  $\epsilon = \frac{1}{2}(F + F^T) - I$ , where  $F^T$  is the transpose of the deformation gradient tensor  $F$  and  $I$  is the identity tensor. This method yields the strain components with atomic resolution.

### B. Charge transfer multiplet calculations

Charge transfer multiplet calculations based on the Cowan-Butler-Thole code<sup>48–50</sup> were performed to attribute the valence contributions of each spectrum. The spectra were calculated from the sum of all possible excitations of an electron from the occupied  $2p$  to unoccupied  $3d$  states ( $2p^6 3d^n \rightarrow 2p^5 3d^{n+1}$ ). The ground state ( $2p^6 3d^n$ ) is affected by the crystal field,  $3d$  spin-orbit coupling, and  $3d$ - $3d$  electron interaction (multiplet coupling). The final state ( $2p^5 3d^{n+1}$ ) is affected by the crystal field and  $2p$  and  $3d$  spin-orbit coupling,  $2p$ - $3d$  and  $3d$ - $3d$  electron interaction (multiplet coupling). We simulated Co-O covalency using ligand-to-metal charge

transfer, which transitions can be described as  $2p^6 3d^m \underline{L} \rightarrow 2p^5 3d^{m+1} \underline{L}$ , where  $m = n + 1$  and  $\underline{L}$  denotes a hole in the oxygen ligand. The atomic Slater-Condon parameters ( $F_{dd}$ ,  $F_{pd}$ , and  $G_{pd}$ ) were scaled to 80% of the Hartree-Fock values. The calculations were performed with the CTM4XAS interface<sup>51</sup>. The semi-empirical calculation parameters are listed in supplementary section S2. To estimate the valence state contributions to the experimental Co  $L$  edges, linear combination fitting of simulated spectra was performed after subtraction of the step edge. The step edge is typically located a few eV above the white line<sup>52</sup>. Hence, the step edge was subtracted at 3.5 eV above the white line for  $\text{Co}^{2+}$ , 1.5 eV for  $\text{Co}^{3+}$ , and 1.5 for  $\text{Co}^{4+}$  with a ratio of 2:1 for the  $L_3$  and  $L_2$  edge, respectively. The simulated spectra were normalized to the number of holes in the  $3d$  orbitals before linear combination fitting.

### III. RESULTS AND DISCUSSION

To assess the structural quality of the multilayers, we applied a comprehensive set of characterization methods. X-ray diffraction measurements (Figure 2) indicate successful growth of highly crystalline epitaxial multilayers. The  $2\theta$ - $\omega$  scans (Figure 2a) show a complex oscillatory pattern of Laue fringes around the film peak due to interference effects of the layers with slightly different out-of-plane lattice parameters. The presence of the fringes points towards highly crystalline layers with sharp interfaces at the macroscopic scale<sup>53</sup>, consistent with the RHEED patterns (Figure S1). Reciprocal space maps around the 103 reflections (Figure 2b) show that all films are commensurately strained to the substrate. In addition, AFM measurements (Figure S2) show characteristic vicinal step-terraces, also observed for the substrate, with some unit cell height variations.

The Co oxidation state is examined by X-ray absorption spectroscopy. The transition metal  $L$  edges correspond to transitions of electrons from  $2p$  orbitals into empty states. They are dominated by excitations to the empty  $3d$  orbitals ( $2p^6 3d^n \rightarrow 2p^5 3d^{n+1}$ ), which makes the spectra sensitive to the  $d$  orbital occupation of the initial state<sup>54</sup>. Figure 3a shows the Co  $L$  edges of the multilayers and a single 10 nm  $\text{LaCoO}_3$  layer. To attribute the contributions of each valence state to the spectra, we simulated the spectral shape of  $\text{Co}^{2+}$ ,  $\text{Co}^{3+}$  and  $\text{Co}^{4+}$  using charge transfer multiplet calculations (Figure 3b). For  $\text{Co}^{2+}$ , we only consider a HS state as the LS state is induced only by strong Jahn-Teller distortions<sup>55</sup>. As

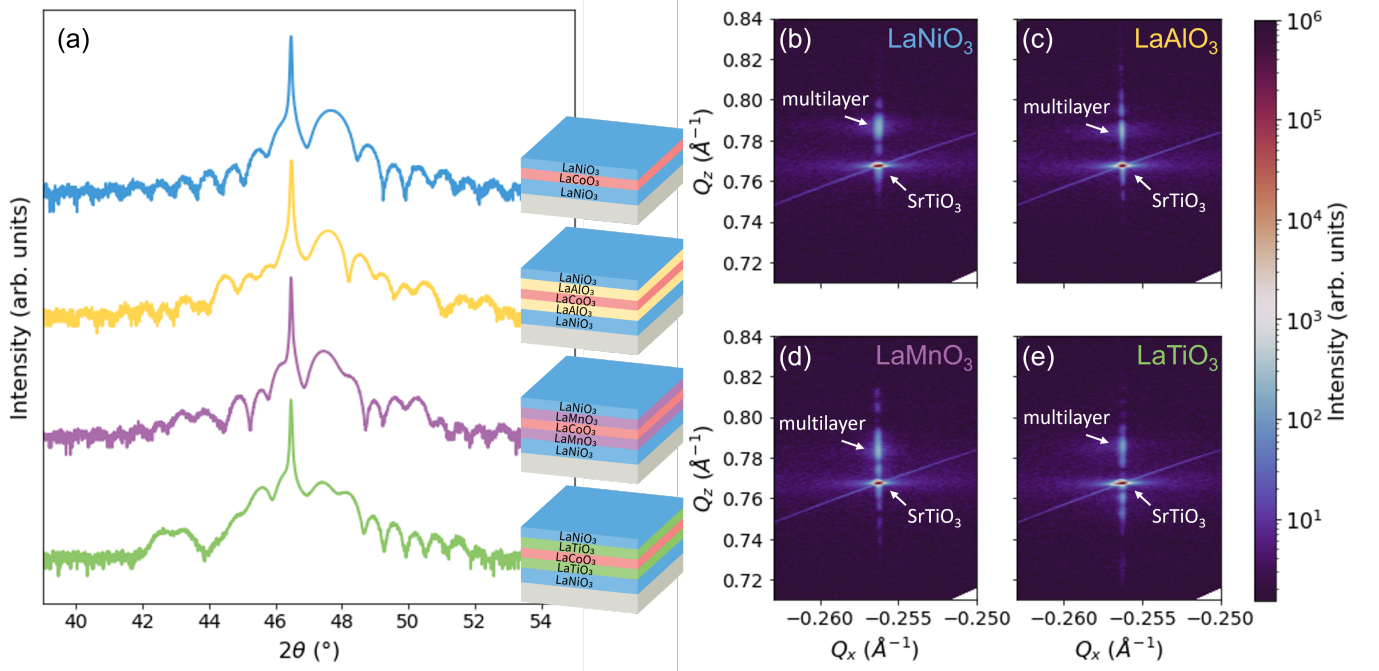


FIG. 2. X-ray diffraction measurements of the LaCoO<sub>3</sub> multilayers: (a)  $2\theta$ - $\omega$  scans. (b) Reciprocal space maps of the 103 reflections of the multilayers containing the (b) LaNiO<sub>3</sub>-LaCoO<sub>3</sub> interface, (c) LaAlO<sub>3</sub>-LaCoO<sub>3</sub> interface, (d) LaMnO<sub>3</sub>-LaCoO<sub>3</sub> interface, (e) LaTiO<sub>3</sub>-LaCoO<sub>3</sub> interface.

Co in LaCoO<sub>3</sub> is reported to contain a mixture of Co<sup>3+</sup> LS and HS<sup>27</sup>, both spin states are considered. For Co<sup>4+</sup> we consider only a HS contribution as the experimental spectrum of SrCoO<sub>3</sub> looks most similar to HS Co<sup>4+</sup><sup>56</sup>. In the HS configuration of  $d^5$ , each orbital would be occupied by one electron in each  $d$  orbital, which is considered to be a likely configuration. A linear combination fitting of these simulated spectra helps to identify differences between samples. However, due to differences between theory and experiment, the concentrations extracted from linear combination fitting serve only as approximate indicators and should not be interpreted as exact values of the Co oxidation states within each sample.

The spectrum obtained for a single 10 nm LaCoO<sub>3</sub> film, shown in red in Figure 3, shows features of multiple oxidation states. Based on the stoichiometry, a Co<sup>3+</sup> oxidation state ( $d^6$ ) is expected for the single layer. While the position of the white line and the shoulder at  $\sim 782$  eV are characteristic for a Co<sup>3+</sup> oxidation state, an additional feature is visible at  $\sim 778$  eV. This feature indicates a small concentration of Co<sup>2+</sup>, often observed for LaCoO<sub>3</sub> surfaces<sup>17,57-59</sup>. This small amount of Co<sup>2+</sup> is likely due to defects in the surface region. Haverkort *et al.* found that LaCoO<sub>3</sub> is an inhomogeneous mixed-spin state system that can be simulated by the sum of Co<sup>3+</sup> LS and HS states. By fitting a linear combination of the simulated spectra for Co<sup>3+</sup> LS and HS and Co<sup>2+</sup> (the dotted line in Figure 3a), we find a slightly higher contribution of HS compared to LS and approximately 6% Co<sup>2+</sup>. This is a larger HS population than reported for LaCoO<sub>3</sub> single crystals<sup>27</sup>, but similar to other LaCoO<sub>3</sub> epitaxial thin films<sup>57,58</sup>. This higher HS population is expected due to the epitaxial strain in the thin film<sup>28</sup>. When creating a LaNiO<sub>3</sub>-LaCoO<sub>3</sub> interface, the white line of

the  $L_3$  shifts  $\sim 0.2$  eV to higher photon energies as shown in blue in Figure 3. Furthermore, the shoulder at  $\sim 782$  eV is less pronounced. Based on the predictive spectral shapes using CTM calculations (Figure 3b), the LaNiO<sub>3</sub>-LaCoO<sub>3</sub> interface could either be the result of a different Co<sup>3+</sup> LS/HS population, or contain some Co<sup>4+</sup> contribution. The shift of the white line is indicative of a higher oxidation state. The difference in the  $L_3$  white line position is  $\sim 0.3$  eV for LaCoO<sub>3</sub> (Co<sup>3+</sup>) and SrCoO<sub>3</sub> (Co<sup>4+</sup>)<sup>60,61</sup>. Therefore, the small shift for the LaNiO<sub>3</sub>-LaCoO<sub>3</sub> interface points towards some Co<sup>4+</sup> population. A linear combination fit with and without the Co<sup>4+</sup> component shown in Figure S3b and c, respectively. The linear combination fit without the Co<sup>4+</sup> component shows a mismatch in the white line position as well as a discrepancy in spectral shape. Including a small amount of Co<sup>4+</sup> ( $\sim 14\%$ ) results in a better match with the experimental data. This points towards a partial Co  $d^5$  orbital occupation in proximity of the LaNiO<sub>3</sub>-LaCoO<sub>3</sub> interface. If this partial  $d^5$  occupation would be due to interfacial charge transfer from Co to Ni, a Ni<sup>2+</sup> oxidation state is expected close to the interface. Due to the overlap between the La  $M_4$  and the Ni  $L_3$  edge, we were not able to resolve the Ni oxidation state using XAS.

To block the interaction between the LaNiO<sub>3</sub> and LaCoO<sub>3</sub> layers, we employed a LaAlO<sub>3</sub> spacer layer. The resulting spectrum in Figure 3a in yellow, shows a predominantly Co<sup>3+</sup> LS ( $\sim 90\%$ ) spectral shape. Hence, we conclude that the LaAlO<sub>3</sub> spacer layer successfully blocks electron transfer from Co to Ni. This predominantly LS state is unexpected for LaCoO<sub>3</sub> thin films at room temperature<sup>28</sup>. A similar effect was observed by Jeong *et al.*<sup>32</sup> in LaCoO<sub>3</sub>-LaAlO<sub>3</sub> superlattices, where the authors attribute a Co<sup>3+</sup> LS state to the reduction

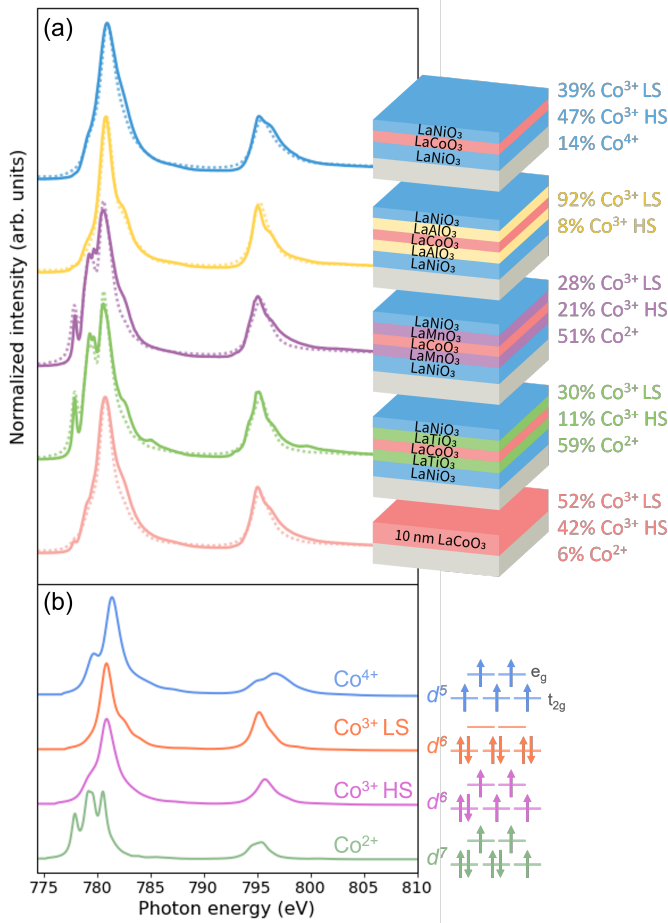


FIG. 3. (a) Co  $L_{2,3}$  edges for different LaCoO<sub>3</sub> and a 10 nm single LaCoO<sub>3</sub> film (solid lines). Dashed lines represent a linear combination fit of the simulated spectra. (b) Simulated Co  $L_{2,3}$  edges for different valence and spin states.

of dimensionality. This observation will be revisited in the STEM analysis.

A partial Co  $d^7$  occupation is expected for the LaTiO<sub>3</sub>-LaCoO<sub>3</sub> interface due to electron transfer from Ti to Co<sup>15</sup>. By comparison of the experimental spectra with the simulated Co<sup>2+</sup> spectrum, it is evident that the LaTiO<sub>3</sub>-LaCoO<sub>3</sub> interface contains a high Co<sup>2+</sup> population. Furthermore, the white line shifts to slightly lower photon energies ( $\sim 0.2$  eV). The small contributions at  $\sim 785$  and  $799.5$  eV are most likely originating from the  $M_{4,5}$  edge of a small Ba contamination in the LaTiO<sub>3</sub> layer. A linear combination fit of simulated spectra results in an approximate concentration of  $\sim 59\%$  Co<sup>2+</sup>. As shown in Figure 3, the linear combination deviates slightly in spectral shape from the experimental data due to the relative intensity of the peaks in the simulated Co<sup>2+</sup> spectrum. These discrepancies are strongly dependent on broadening of the theoretical spectra and are consistent with literature<sup>54,62,63</sup>. Qualitatively, the partial  $d^7$  occupation is in agreement with the expected charge transfer from Ti to Co across this interface<sup>15,17</sup>. However, a 100% Co<sup>2+</sup> population was reported for a 4 u.c. thick LaCoO<sub>3</sub> layer between LaTiO<sub>3</sub>

by Araizi-Kanoutas *et al.*<sup>17</sup>, while we find a lower Co<sup>2+</sup> population ( $\sim 59\%$ ). Two potential factors may account for this discrepancy. First of all, the oxygen vacancy content in LaCoO<sub>3</sub> is expected to be lower in this work due to the growth pressure, which is two orders of magnitude higher in this work. Second, charge transfer between LaTiO<sub>3</sub> and LaNiO<sub>3</sub> can result in less charge transfer at the LaTiO<sub>3</sub>-LaCoO<sub>3</sub> interface. Charge transfer between LaTiO<sub>3</sub> and LaNiO<sub>3</sub> is expected, as was previously reported by Disa *et al.*<sup>12</sup>, leaving fewer electrons to transfer from LaTiO<sub>3</sub> to LaCoO<sub>3</sub>. When blocking charge transfer between LaTiO<sub>3</sub> and LaNiO<sub>3</sub> with a LaAlO<sub>3</sub> interlayer, we find an approximate population of  $\sim 68\%$  Co<sup>2+</sup> (Figure S4). This confirms that the interaction between LaTiO<sub>3</sub> and LaNiO<sub>3</sub> influences charge transfer at the LaTiO<sub>3</sub>-LaCoO<sub>3</sub> interface. However, even when blocking the interaction between LaTiO<sub>3</sub> and LaNiO<sub>3</sub>, we find a substantially lower  $d^7$  population than found with different PLD conditions in prior work<sup>17</sup>.

In contrast to the LaTiO<sub>3</sub>-LaCoO<sub>3</sub> interface, where LaTiO<sub>3</sub> has a high propensity of overoxidizing<sup>19,20</sup>, the LaMnO<sub>3</sub>-LaCoO<sub>3</sub> can be grown at relatively high deposition pressures (0.1 mbar). Due to the high deposition pressure, oxygen vacancies should play a smaller role in the  $d$  orbital occupation at this interface. A strong Co<sup>2+</sup> fingerprint for this interface can be observed in Figure 3a. Linear combination fitting of simulated spectra results in a slightly lower Co<sup>2+</sup> concentration for this interface ( $\sim 51\%$ ) compared to the LaTiO<sub>3</sub>-LaCoO<sub>3</sub> interface ( $\sim 59\%$ ). As the O 2p band centers are closer for LaMnO<sub>3</sub> and LaCoO<sub>3</sub> compared to LaTiO<sub>3</sub> and LaCoO<sub>3</sub>, a smaller amount of interfacial charge transfer and therefore a lower  $d^7$  population is expected for this interface<sup>15</sup>. Furthermore, the Co<sup>2+</sup> fingerprint around 779.2 and 779.8 eV shows a difference in relative intensity compared to the LaTiO<sub>3</sub>-LaCoO<sub>3</sub> interface. This is most likely due to a difference in the Co<sup>3+</sup> HS contribution, which has a shoulder around 779.5 eV (Figure 3b).

To investigate whether the additional electrons in the LaCoO<sub>3</sub> layer originate from the LaMnO<sub>3</sub> layer, we examined the Mn  $L_{2,3}$  edges for this sample, as well for a 4 u.c. LaCoO<sub>3</sub>- 5 u.c. LaMnO<sub>3</sub> - 4 u.c. LaCoO<sub>3</sub> multilayer and a 10 nm LaMnO<sub>3</sub> single layer (Figure S5). We observe a partial Mn<sup>4+</sup> occupation by XAS as discussed in supplementary section S4, confirming charge transfer from Mn to Co.

To further examine the origin of the Co valence state close to the interface with different transition metals, we employed STEM to image the interfaces with atomic resolution. EELS (Figure S6-S8) was used to assess the electronic state with spatial resolution. For all samples, the top LaNiO<sub>3</sub> layer is likely damaged by X-ray irradiation and lamella preparation and should be merely seen as a protective layer.

The EELS maps (Figure S6) show a rather homogeneous spectral shape for the Co  $L$  edge within the signal-to-noise ratio over the thickness of the LaCoO<sub>3</sub> layers for all samples. The Co EELS spectra integrated over the full LaCoO<sub>3</sub> layer (Figure S7) show roughly the same trend in Co oxidation state as the XAS results (Figure 3), though with markedly lower signal-to-noise in the EELS data. The spectral weight of the Co  $L_3$  edge has higher intensity at lower electron energy loss



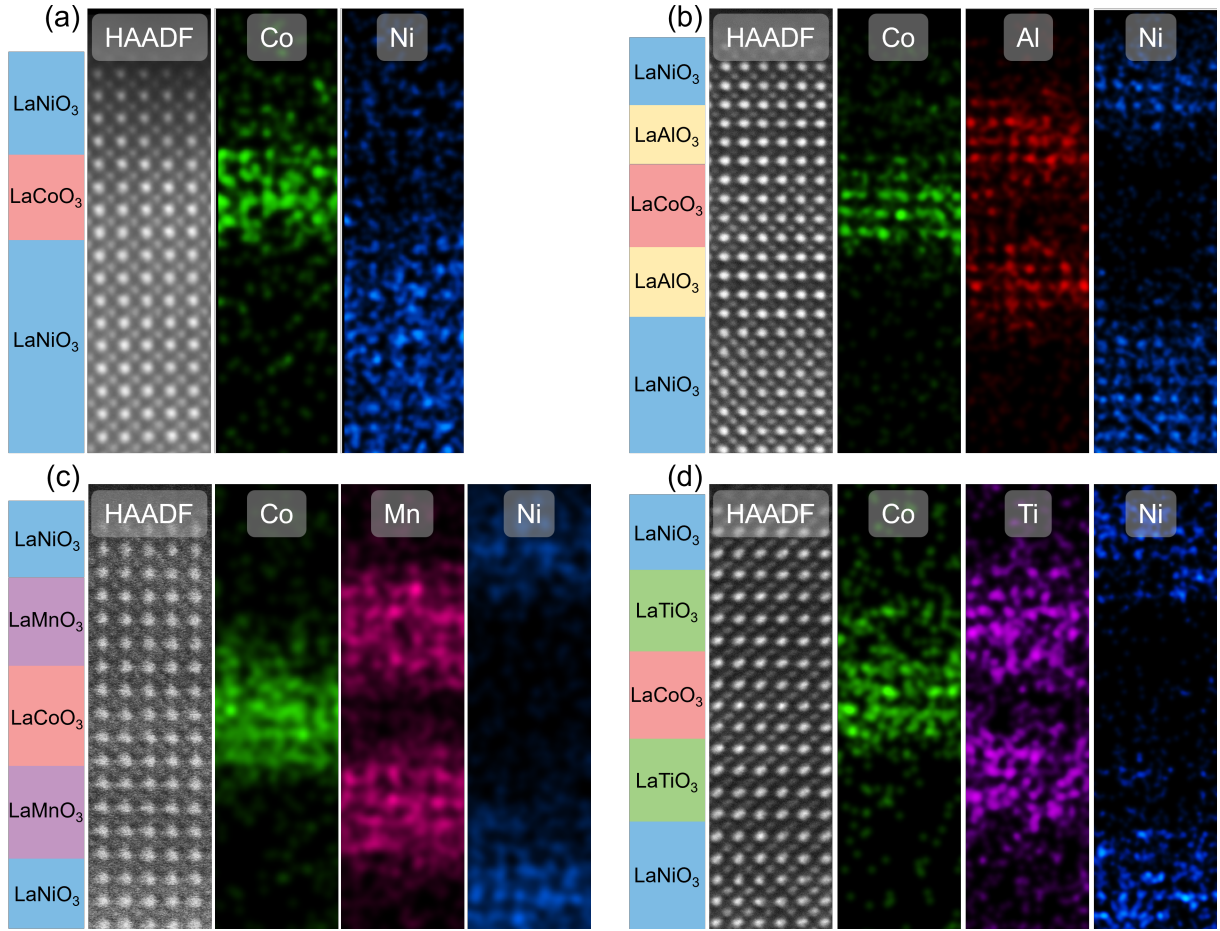


FIG. 4. HAADF STEM images and EDX maps of the multilayers containing the (a)  $\text{LaNiO}_3$ - $\text{LaCoO}_3$  interface, (b)  $\text{LaAlO}_3$ - $\text{LaCoO}_3$  interface, (c)  $\text{LaMnO}_3$ - $\text{LaCoO}_3$  interface, (d)  $\text{LaTiO}_3$ - $\text{LaCoO}_3$  interface.

energies for the samples containing  $\text{LaTiO}_3$  and  $\text{LaMnO}_3$  compared to the samples with the  $\text{LaAlO}_3$  and  $\text{LaNiO}_3$  interfaces, confirming the substantial  $\text{Co}^{2+}$  contribution in these samples.

The valence states of the transition metals on the other side of the interfaces are also in line with the XAS results. For the sample with the  $\text{LaNiO}_3$ - $\text{LaCoO}_3$  interface, the Ni  $L_3$  edge overlaps with the La  $M_4$  edge, making it difficult to assess the Ni oxidation state. Hence, electron transfer from Co to Ni across the interface cannot be confirmed.

The EELS Mn  $L$  edge of the sample with the  $\text{LaMnO}_3$ - $\text{LaCoO}_3$  interface is rather homogeneous over the thickness of the  $\text{LaMnO}_3$  layers (Figure S6c). The integrated spectrum over the bottom  $\text{LaMnO}_3$  layer (Figure S7b) matches the XAS spectrum collected for this sample (Figure S5), implying a partial  $\text{Mn}^{4+}$  oxidation state and confirming charge transfer from Mn to Co.

For the sample with the  $\text{LaTiO}_3$ - $\text{LaCoO}_3$  interface, the Ti EELS signal extends into the  $\text{LaCoO}_3$  layer (Figure S6d), pointing towards substantial intermixing for this sample. However, both the Co spectral shape and Ti spectral shape observed with EELS seem rather homogeneous within the signal-to-noise ratio as a function of position. The four

peaks in the integrated Ti  $L$  edge trace (Figure S7c) indicate a primarily  $\text{Ti}^{4+}$  oxidation state throughout the structure. Hence, it is likely that the  $d^7$  orbital occupation of Co is due to electron transfer from Ti, which is in line with previous work<sup>17</sup>.

The spatial resolution of EELS also enables us to assess the O  $K$  edge per layer (Figure S8). Its spectral shape provides information about the hybridized TM  $3d$  states and their orbital occupation<sup>64,65</sup>. However, the O  $K$  edges in the  $\text{LaCoO}_3$  layer show similar spectral shapes as the neighboring layers, as discussed in detail in supplementary section S5.

Figure 4 shows HAADF STEM images for the four interfaces of interest with high-resolution EDX to identify any intermixing at the interfaces. Most interfaces show minimal intermixing within a single unit cell corresponding to the layer roughness during growth. Interestingly, intermixing seems slightly more pronounced at the top of the  $\text{LaCoO}_3$  layer for all samples, indicating that the  $\text{LaCoO}_3$  migrates into the layer above. This is in line with previous observations<sup>66</sup>. The sample with the  $\text{LaAlO}_3$ - $\text{LaCoO}_3$  interfaces (Figure 4b) shows a small amount of intermixing of Al into the  $\text{LaCoO}_3$ , barely above the noise level. Substantial mixing of Al in the

LaCoO<sub>3</sub> structure could result in a change in spin state as LaAl<sub>1-x</sub>Co<sub>x</sub>O<sub>3</sub> with  $x = 0.3 - 0.5$  has been reported to show a decrease in Co<sup>3+</sup> HS compared to LaCoO<sub>3</sub> due to an increase in the crystal field splitting energy<sup>67</sup>. However, cation intermixing alone cannot explain the almost full Co<sup>3+</sup> LS state observed in the multilayer, as the HS state is expected to be populated even for 50% Al substitution<sup>67</sup> - well beyond the small observable intermixing in Figure 4b.

For the sample with the LaTiO<sub>3</sub>-LaCoO<sub>3</sub> interface, EDX shows a limited amount of intermixing of Ti into the LaCoO<sub>3</sub> layer, which is in line with the EELS results, indicating that mixing of the cations may substantially contribute to the charge transfer in this sample.

The sample with the LaMnO<sub>3</sub>-LaCoO<sub>3</sub> interface (Figure 4c) shows a small amount of cation intermixing between LaCoO<sub>3</sub> and the top LaMnO<sub>3</sub> layer. Electron transfer from Co to Mn is previously reported in LaMn<sub>1-x</sub>Co<sub>x</sub>O<sub>3</sub><sup>62</sup>. Hence, the observed Co<sup>2+</sup> contribution in XAS can originate (partially) from intermixing at this interface<sup>66</sup>.

As discussed above, EELS indicates that the cation *L* edges are rather homogeneous in spectral shape over the layer thicknesses and similar for the top and bottom interfaces, while intermixing is stronger close to the interfaces, implying that the charge transfer extends further than intermixing. Thus, the spatial extent of the electronic effect exceeds that of the chemical intermixing, emphasizing that the observed orbital occupancies and spin states result from an intrinsic interfacial phenomenon governed by electronic—not compositional—length scales, and pointing to electronic driving forces.

While differences in Co valence state can be explained by interfacial charge transfer, the origin of variations in spin remain unclear. Strain analysis reveals more insight into the possible origin of the variations in Co spin states for the different interfaces. All thin films are commensurately tensile strained to the SrTiO<sub>3</sub> substrate, resulting in the same in-plane lattice parameter (Figure 2b-e). Typically, tensile strain reduces the out-of-plane lattice parameter resulting in negative out-of-plane strain. Strain analysis by STEM (Figure 5) shows that the out-of-plane strain deviates for the different interfaces. The largest negative out-of-plane strain is observed for the sample with the LaNiO<sub>3</sub>-LaCoO<sub>3</sub> interface, which contains a high amount of Co<sup>3+</sup> HS concentration. Upon creation of a LaAlO<sub>3</sub>-LaCoO<sub>3</sub> interface, the out-of-plane strain in the LaCoO<sub>3</sub> layer becomes substantially smaller and a primarily Co<sup>3+</sup> LS population is observed. When comparing the samples with the LaMnO<sub>3</sub>-LaCoO<sub>3</sub> and LaTiO<sub>3</sub>-LaCoO<sub>3</sub> interfaces, both having a large Co<sup>2+</sup> HS population, we observe a similar effect for the Co<sup>3+</sup> spin state. The Co<sup>3+</sup> population has relatively more HS for the LaMnO<sub>3</sub>-LaCoO<sub>3</sub> interface, which exhibits more negative out-of-plane strain in the LaCoO<sub>3</sub> layer. Thus, we observe that LaCoO<sub>3</sub> layers with negative out-of-plane strain have more Co<sup>3+</sup> HS, and samples with little out-of-plane strain have more Co<sup>3+</sup> LS.

The Co<sup>3+</sup> spin state is known to be closely related to strain<sup>28,29,31,68</sup>. Tetragonal distortions due to in-plane tensile strain are known to lift the degeneracy of the 3*d* orbitals, thereby decreasing the crystal field splitting energy and favoring Co<sup>3+</sup> HS population. The observed out-of-plane strain for

the samples showing more Co<sup>3+</sup> HS (LaNiO<sub>3</sub>-LaCoO<sub>3</sub> and LaMnO<sub>3</sub>-LaCoO<sub>3</sub> interfaces) points towards such a tetragonal distortion that decreases the crystal field splitting energy and results in a favored HS population. For the samples that show more Co<sup>3+</sup> LS (LaAlO<sub>3</sub>-LaCoO<sub>3</sub> and LaTiO<sub>3</sub>-LaCoO<sub>3</sub> interfaces), contrary to the usual epitaxial strain response, we find minimal negative out-of-plane strain. This leads to a higher crystal field splitting energy compared to the HS samples, which favors occupation of the t<sub>2g</sub> orbitals over the e<sub>g</sub> orbitals and thereby a Co<sup>3+</sup> LS state.

Thus, strain analysis combined with spectroscopy of a set of LaBO<sub>3</sub>-LaCoO<sub>3</sub> interfaces points towards the importance of structural distortions and strain relaxation mechanisms in the *d* orbital occupation of Co in LaCoO<sub>3</sub>. Strain relaxation provides an alternative argument to the dimensionality argument provided by Jeong *et al.*<sup>32</sup>. In their work, the authors observed a predominantly Co<sup>3+</sup> LS state in LaAlO<sub>3</sub>-LaCoO<sub>3</sub> superlattices as the reduced dimensionality of the LaCoO<sub>3</sub> layers between insulating LaAlO<sub>3</sub> increased the crystal field splitting energy compared to the bulk.

Unfortunately, the exact nature of the LS state in our multilayers remains unknown without further investigation of the strain relaxation mechanism. Nevertheless, these findings demonstrate that the electronic ground state (oxidation state and spin state) in correlated oxide interfaces cannot be understood from charge transfer or dimensionality alone; rather, it emerges from the coupled evolution of strain, symmetry distortion, and interfacial structural accommodation.

#### IV. CONCLUSIONS

We demonstrated control over the *d* orbital occupation in LaCoO<sub>3</sub> by the use of interfacial engineering. Using CTM calculations to interpret the Co *L* edges, we observe a partial *d*<sup>7</sup> occupation at the interface with LaTiO<sub>3</sub>. A partial *d*<sup>7</sup> orbital occupation is also formed at the interface with LaMnO<sub>3</sub>, which does not show the same tendency to overoxidize as LaTiO<sub>3</sub>. Hereby, we confirm that oxygen nonstoichiometry is not the main driving force of charge transfer at these isopolar interfaces. Furthermore, we found a partial Co *d*<sup>5</sup> occupation at the interface with LaNiO<sub>3</sub>, and blocking of this charge transfer with a LaAlO<sub>3</sub> layer. Aside from a change in valence state due to interfacial charge transfer, we observe a change in spin state for the different interfaces. Strain analysis of high-resolution STEM images points towards a correlation between out-of-plane strain and the Co<sup>3+</sup> spin state, identifying that structural distortions - in addition to reduced dimensionality and interfacial charge transfer - dictate the spin-state of LaCoO<sub>3</sub>, underscoring the multifaceted nature of electronic reconstruction at oxide interfaces. Control over the *d* orbital occupancy through interfacial engineering offers a powerful and underappreciated design strategy for oxide electronics and (electro)catalysis, where the outer-electron orbital occupancy and spin states dictate key material properties and functionality.

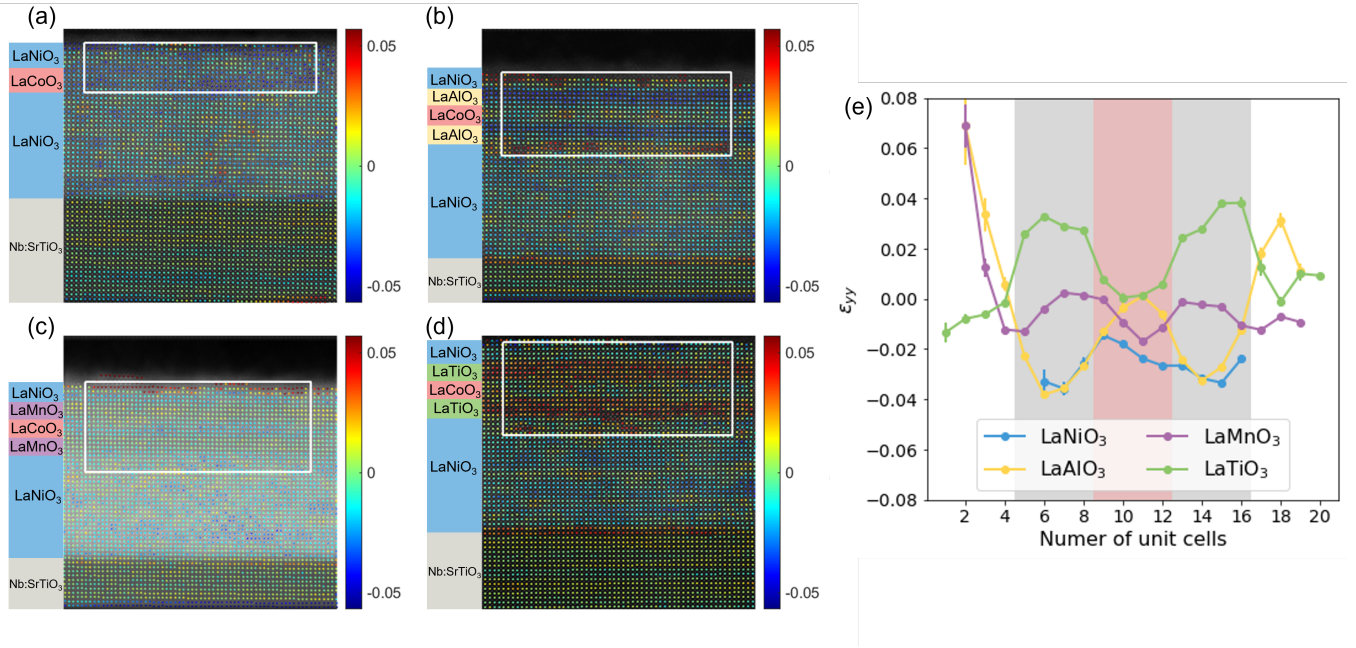


FIG. 5. Out-of-plane strain mapping of the multilayers containing the (a) LaNiO<sub>3</sub>-LaCoO<sub>3</sub> interface, (b) LaAlO<sub>3</sub>-LaCoO<sub>3</sub> interface, (c) LaMnO<sub>3</sub>-LaCoO<sub>3</sub> interface, (d) LaTiO<sub>3</sub>-LaCoO<sub>3</sub> interface. White outlined regions are used to calculate the average out of plane strain per layer. (e) Average out of plane strain as a function of distance from the interface. Averaging is performed horizontally across the white area outlined in (a)-(d). The LaCoO<sub>3</sub> layer is indicated by the red shaded region, while the neighboring layers are indicated by the grey shaded region. The white region corresponds to the LaNiO<sub>3</sub>. Error bars indicate standard errors. The legend labels indicate the neighboring layer to the LaCoO<sub>3</sub> layer.

## ACKNOWLEDGMENTS

This work is funded by the Netherlands Ministry of Economic Affairs' Top Consortia for Knowledge and Innovation (TKIs) Allowance (CHEMIE.PGT.2021.007). This work was carried out with the support of Diamond Light Source, instruments B07-B and B07-C (proposal SI33107 and cm31118). The authors thank Pilar Ferrer for her support during the XAS experiments. The authors thank Guido Mul for fruitful discussions.

## AUTHOR CONTRIBUTIONS

E.K. synthesized the samples and performed RHEED, XRD and AFM measurements. E.K., E.M., I.B. and M.S. performed XAS measurements. E.K. performed CTM simulations and analysed the XAS data. F.G. supervised the simulations and XAS data analysis. N.G. performed STEM measurements. N.G., Z.Z. and A.A. analysed EDX and EELS data. J.V. supervised the EELS/EDX analysis. A.D.B. performed STEM strain analysis. S.V.A. supervised the STEM strain analysis. C.B., B.M. and G.K. conceptualized the project and supervised the research. E.K. wrote the manuscript with contributions from all authors. All authors discussed the results and contributed to the final version.

## REFERENCES

- <sup>1</sup>Y. Tokura and N. Nagaosa, "Orbital Physics in Transition-Metal Oxides," *Science* **288**, 462–468 (2000).
- <sup>2</sup>J. B. Goodenough, "Perspective on Engineering Transition-Metal Oxides," *Chemistry of Materials* **26**, 820–829 (2014).
- <sup>3</sup>J. Mannhart and D. G. Schlom, "Oxide Interfaces—An Opportunity for Electronics," *Science* **327**, 1607–1611 (2010).
- <sup>4</sup>H. Y. Hwang, Y. Iwasa, M. Kawasaki, B. Keimer, N. Nagaosa, and Y. Tokura, "Emergent phenomena at oxide interfaces," *Nat. Mater.* **11**, 103–113 (2012).
- <sup>5</sup>Z. Liao, M. Huijben, Z. Zhong, N. Gauquelin, S. Macke, R. J. Green, S. V. Aert, J. Verbeeck, G. V. Tendeloo, K. Held, G. A. Sawatzky, G. Koster, and G. Rijnders, "Controlled lateral anisotropy in correlated manganite heterostructures by interface-engineered oxygen octahedral coupling," *Nature Mater* **15**, 425–431 (2016).
- <sup>6</sup>P. Liu and X. Ning, "High-spin state and magnetic coupling induced through interfacial orbital reconstruction observed in SrRuO<sub>3</sub>/LaNiO<sub>3</sub> superlattice," *Materials Research Letters* **8**, 173–179 (2020).
- <sup>7</sup>M. Li, C. Tang, T. R. Paudel, D. Song, W. Lü, K. Han, Z. Huang, S. Zeng, X. Renshaw Wang, P. Yang, Ariando, J. Chen, T. Venkatesan, E. Y. Tsymbal, C. Li, and S. J. Pennycook, "Controlling the Magnetic Properties of LaMnO<sub>3</sub>/SrTiO<sub>3</sub> Heterostructures by Stoichiometry and Electronic Reconstruction: Atomic-Scale Evidence," *Advanced Materials* **31**, 1901386 (2019).
- <sup>8</sup>Y. Ji, S. Hu, J. Liu, L. Wei, C. Luo, V. Ukleev, F. Radu, W. Yan, D. Chen, Z. Zhong, Y. Gan, K. Chen, and Z. Liao, "High-temperature ferromagnetic LaCoO<sub>3</sub> triggered by interfacial electron transfer and exchange coupling," *Phys. Rev. B* **109**, 174423 (2024).
- <sup>9</sup>X. Guan, X. Shen, J. Zhang, W. Wang, J. Zhang, H. Wang, W. Wang, Y. Yao, J. Li, C. Gu, J. Sun, and R. Yu, "Tuning magnetism and crystal orientations by octahedral coupling in LaCoO<sub>3</sub>/LaMnO<sub>3</sub> thin films," *Phys. Rev. B* **100**, 014427 (2019).

- <sup>10</sup>J. Hoffman, I. C. Tung, B. B. Nelson-Cheeseman, M. Liu, J. W. Freeland, and A. Bhattacharya, "Charge transfer and interfacial magnetism in  $(\text{LaNiO}_3)_n/(\text{LaMnO}_3)_2$  superlattices," *Phys. Rev. B* **88**, 144411 (2013).
- <sup>11</sup>Y. Cao, X. Liu, M. Kareev, S. Middey, D. Meyers, J.-W. Kim, P. J. Ryan, J. W. Freeland, and J. Chakhalian, "Engineered Mott ground state in a  $\text{LaTiO}_{3+\delta}/\text{LaNiO}_3$  heterostructure," *Nat Commun* **7**, 10418 (2016).
- <sup>12</sup>A. S. Disa, D. P. Kumah, A. Malashevich, H. Chen, D. A. Arena, E. D. Specht, S. Ismail-Beigi, F. J. Walker, and C. H. Ahn, "Orbital Engineering in Symmetry-Breaking Polar Heterostructures," *Phys. Rev. Lett.* **114**, 026801 (2015).
- <sup>13</sup>H. Chen and A. Millis, "Charge transfer driven emergent phenomena in oxide heterostructures," *Journal of Physics: Condensed Matter* **29**, 243001 (2017).
- <sup>14</sup>X. Ding, B. Yang, H. Leng, J. H. Jang, J. Zhao, C. Zhang, S. Zhang, G. Cao, J. Zhang, R. Mishra, J. Yi, D. Qi, Z. Gai, X. Zu, S. Li, B. Huang, A. Borisovich, and L. Qiao, "Crystal Symmetry Engineering in Epitaxial Perovskite Superlattices," *Advanced Functional Materials* **31**, 2106466 (2021).
- <sup>15</sup>Z. Zhong and P. Hansmann, "Band Alignment and Charge Transfer in Complex Oxide Interfaces," *Phys. Rev. X* **7**, 011023 (2017).
- <sup>16</sup>M. Huijben, A. Brinkman, G. Koster, G. Rijnders, H. Hilgenkamp, and D. H. A. Blank, "Structure-Property Relation of  $\text{SrTiO}_3/\text{LaAlO}_3$  Interfaces," *Advanced Materials* **21**, 1665–1677 (2009).
- <sup>17</sup>G. Arazi-Kanoutas, J. Geessinck, N. Gauquelin, S. Smit, X. H. Verbeeck, S. K. Mishra, P. Bencok, C. Schlueter, T.-L. Lee, D. Krishnan, J. Fatermans, J. Verbeeck, G. Rijnders, G. Koster, and M. S. Golden, "Co valence transformation in isopolar  $\text{LaCoO}_3/\text{LaTiO}_3$  perovskite heterostructures via interfacial engineering," *Phys. Rev. Mater.* **4**, 026001 (2020).
- <sup>18</sup>J. E. Kleibecker, Z. Zhong, H. Nishikawa, J. Gabel, A. Müller, F. Pfaff, M. Sing, K. Held, R. Claessen, G. Koster, and G. Rijnders, "Electronic Reconstruction at the Isopolar  $\text{LaTiO}_3/\text{LaFeO}_3$  Interface: An X-Ray Photoemission and Density-Functional Theory Study," *Phys. Rev. Lett.* **113**, 237402 (2014).
- <sup>19</sup>P. Scheiderer, M. Schmitt, J. Gabel, M. Zapf, M. Stübinger, P. Schütz, L. Dudy, C. Schlueter, T.-L. Lee, M. Sing, and R. Claessen, "Tailoring Materials for Motttronics: Excess Oxygen Doping of a Prototypical Mott Insulator," *Advanced Materials* **30**, 1706708 (2018).
- <sup>20</sup>A. Ohtomo, D. A. Muller, J. L. Grazul, and H. Y. Hwang, "Epitaxial growth and electronic structure of  $\text{LaTiO}_x$  films," *Applied Physics Letters* **80**, 3922–3924 (2002).
- <sup>21</sup>M. A. Korotin, S. Y. Ezhov, I. V. Solov'yev, V. I. Anisimov, D. I. Khomskii, and G. A. Sawatzky, "Intermediate-spin state and properties of  $\text{LaCoO}_3$ ," *Phys. Rev. B* **54**, 5309–5316 (1996).
- <sup>22</sup>V. G. Bhide, D. S. Rajoria, G. R. Rao, and C. N. R. Rao, "Mössbauer Studies of the High-Spin-Low-Spin Equilibria and the Localized-Collective Electron Transition in  $\text{LaCoO}_3$ ," *Phys. Rev. B* **6**, 1021–1032 (1972).
- <sup>23</sup>T. Kyömen, Y. Asaka, and M. Itoh, "Negative cooperative effect on the spin-state excitation in  $\text{LaCoO}_3$ ," *Phys. Rev. B* **67**, 144424 (2003).
- <sup>24</sup>C. S. Naiman, R. Gilmore, B. DiBartolo, A. Linz, and R. Santoro, "Interpretation of the Magnetic Properties of  $\text{LaCoO}_3$ ," *Journal of Applied Physics* **36**, 1044–1045 (1965).
- <sup>25</sup>P. M. Raccah and J. B. Goodenough, "First-Order Localized-Electron  $\Rightarrow$  Collective-Electron Transition in  $\text{LaCoO}_3$ ," *Phys. Rev.* **155**, 932–943 (1967).
- <sup>26</sup>A. Podlesnyak, S. Streule, J. Mesot, M. Medarde, E. Pomjakushina, K. Conder, A. Tanaka, M. W. Haverkort, and D. I. Khomskii, "Spin-State Transition in  $\text{LaCoO}_3$ : Direct Neutron Spectroscopic Evidence of Excited Magnetic States," *Phys. Rev. Lett.* **97**, 247208 (2006).
- <sup>27</sup>M. W. Haverkort, Z. Hu, J. C. Cezar, T. Burnus, H. Hartmann, M. Reuther, C. Zobel, T. Lorenz, A. Tanaka, N. B. Brookes, H. H. Hsieh, H.-J. Lin, C. T. Chen, and L. H. Tjeng, "Spin State Transition in  $\text{LaCoO}_3$  Studied Using Soft X-ray Absorption Spectroscopy and Magnetic Circular Dichroism," *Phys. Rev. Lett.* **97**, 176405 (2006).
- <sup>28</sup>R.-P. Wang, J. Geessinck, H. Elnaggar, Y. A. Birkhölzer, K. Tomiyasu, J. Okamoto, B. Liu, C.-H. Du, D.-J. Huang, G. Koster, and F. M. F. de Groot, "Low-energy orbital excitations in strained  $\text{LaCoO}_3$  films," *Phys. Rev. B* **100**, 165148 (2019).
- <sup>29</sup>G. E. Sterbinsky, P. J. Ryan, J.-W. Kim, E. Karapetrova, J. X. Ma, J. Shi, and J. C. Woicik, "Local atomic and electronic structures of epitaxial strained  $\text{LaCoO}_3$  thin films," *Phys. Rev. B* **85**, 020403 (2012).
- <sup>30</sup>H. Hsu, P. Blaha, and R. M. Wentzcovitch, "Ferromagnetic insulating state in tensile-strained  $\text{LaCoO}_3$  thin films from LDA +  $U$  calculations," *Phys. Rev. B* **85**, 140404 (2012).
- <sup>31</sup>K. Gupta and P. Mahadevan, "Strain-driven magnetism in  $\text{LaCoO}_3$  thin films," *Phys. Rev. B* **79**, 020406 (2009).
- <sup>32</sup>D. W. Jeong, W. S. Choi, S. Okamoto, J. Kim, K. W. Kim, S. J. Moon, D.-Y. Cho, H. N. Lee, and T. W. Noh, "Dimensionality Control of d-orbital Occupation in Oxide Superlattices," *Scientific Reports* **4**, 6124 (2014).
- <sup>33</sup>J. Suntivich, K. J. May, H. A. Gasteiger, J. B. Goodenough, and Y. Shao-Horn, "A Perovskite Oxide Optimized for Oxygen Evolution Catalysis from Molecular Orbital Principles," *Science* **334**, 1383–1385 (2011).
- <sup>34</sup>E. M. Kiens, M.-J. Choi, L. Wei, Q. Lu, L. Wang, and C. Baeumer, "Deeper mechanistic insights into epitaxial nickelate electrocatalysts for the oxygen evolution reaction," *Chem. Commun.* **59**, 4562–4577 (2023).
- <sup>35</sup>L. Heymann, M. L. Weber, M. Wohlgemuth, M. Risch, R. Dittmann, C. Baeumer, and F. Gunkel, "Separating the Effects of Band Bending and Covalency in Hybrid Perovskite Oxide Electrocatalyst Bilayers for Water Electrolysis," *ACS Applied Materials & Interfaces* **14**, 14129–14136 (2022).
- <sup>36</sup>G. Koster, G. Rijnders, D. H. Blank, and H. Rogalla, "Surface morphology determined by (001) single-crystal  $\text{SrTiO}_3$  termination," *Physica C: Superconductivity* **339**, 215–230 (2000).
- <sup>37</sup>J. Fowlie, C. Lichtensteiger, M. Gibert, H. Meley, P. Willmott, and J.-M. Triscone, "Thickness-Dependent Perovskite Octahedral Distortions at Heterointerfaces," *Nano Letters* **19**, 4188–4194 (2019).
- <sup>38</sup>C. Baeumer, "Tuning electrochemically driven surface transformation in atomically flat  $\text{LaNiO}_3$  thin films for enhanced water electrolysis," *Nature Materials* **20**, 674–682 (2021).
- <sup>39</sup>D. C. Grinter, P. Ferrer, F. Venturini, M. A. van Spronsen, A. I. Large, S. Kumar, M. Jaugstetter, A. Iordachescu, A. Watts, S. L. M. Schroeder, A. Kroner, F. Grillo, S. M. Francis, P. B. Webb, M. Hand, A. Walters, M. Hillman, and G. Held, "VerSoX B07-B: a high-throughput XPS and ambient pressure NEXAFS beamline at Diamond Light Source," *Journal of Synchrotron Radiation* **31**, 578–589 (2024).
- <sup>40</sup>E. Grieten, O. Schalm, P. Tack, S. Bauters, P. Storme, N. Gauquelin, J. Caen, A. Patelli, L. Vincze, and D. Schryvers, "Reclaiming the image of daguerreotypes: Characterization of the corroded surface before and after atmospheric plasma treatment," *Journal of Cultural Heritage* **28**, 56–64 (2017).
- <sup>41</sup>B. Conings, S. A. Bretschneider, A. Babayigit, N. Gauquelin, I. Cardinaletti, J. Manca, J. Verbeeck, H. J. Snaith, and H.-G. Boyen, "Structure-Property Relations of Methylamine Vapor Treated Hybrid Perovskite  $\text{CH}_3\text{NH}_3\text{PbI}_3$  Films and Solar Cells," *ACS Applied Materials & Interfaces* **9**, 8092–8099 (2017).
- <sup>42</sup>D. J. Groenendijk, C. Autieri, T. C. van Thiel, W. Brzezicki, J. R. Hortensius, D. Afanasiev, N. Gauquelin, P. Barone, K. H. W. van den Bos, S. van Aert, J. Verbeeck, A. Filippetti, S. Picozzi, M. Cuoco, and A. D. Caviglia, "Berry phase engineering at oxide interfaces," *Phys. Rev. Res.* **2**, 023404 (2020).
- <sup>43</sup>J. Verbeeck *et al.*, "pyEELSMODEL: Python library for model-based EELS quantification," *BIO Web of Conferences* **129**, 10035 (2024).
- <sup>44</sup>W. Van den Broek, D. Jannis, and J. Verbeeck, "Convexity constraints on linear background models for electron energy-loss spectra," *Ultramicroscopy* **254**, 113830 (2023).
- <sup>45</sup>Z. Zhang, I. Lobato, H. Brown, D. Lamoën, D. Jannis, J. Verbeeck, S. Van Aert, and P. D. Nellist, "Relativistic EELS scattering cross-sections for microanalysis based on Dirac solutions," *Ultramicroscopy* **269**, 114083 (2025).
- <sup>46</sup>Z. Zhang, I. Lobato, S. van Aert, and P. Nellist, "Superalign: a multi-frame alignment tool for multi-modal microscopy dataset," To be submitted.
- <sup>47</sup>A. De Backer, K. van den Bos, W. Van den Broek, J. Sijbers, and S. Van Aert, "StatSTEM: An efficient approach for accurate and precise model-based quantification of atomic resolution electron microscopy images," *Ultramicroscopy* **171**, 104–116 (2016).
- <sup>48</sup>R. Cowan, *The Theory of Atomic Structure and Spectra*, Los Alamos Series in Basic and Applied Sciences (University of California Press, 1981).
- <sup>49</sup>B. Thole, G. Van Der Laan, and P. Butler, "Spin-mixed ground state of Fe phthalocyanine and the temperature-dependent branching ratio in X-ray absorption spectroscopy," *Chemical Physics Letters* **149**, 295–299 (1988).



- <sup>50</sup>P. Butler, *Point Group Symmetry Applications: Methods and Tables* (Springer US, 2012).
- <sup>51</sup>E. Stavitski and F. M. de Groot, "The CTM4XAS program for EELS and XAS spectral shape analysis of transition metal L edges," *Micron* **41**, 687–694 (2010).
- <sup>52</sup>G. van der Laan, J. Zaanen, G. A. Sawatzky, R. Karnatak, and J.-M. Esteve, "Comparison of X-ray absorption with X-ray photoemission of nickel dihalides and NiO," *Phys. Rev. B* **33**, 4253–4263 (1986).
- <sup>53</sup>R. James, *The Optical Principles of the Diffraction of X-rays*, Originally publ. as *The Crystalline State*, Vol. 2 in 1948 (Ox Bow Press, 1982).
- <sup>54</sup>F. M. de Groot, H. Elnaggar, F. Frati, R. Pan Wang, M. U. Delgado-Jaime, M. van Veenendaal, J. Fernandez-Rodriguez, M. W. Haverkort, R. J. Green, G. van der Laan, Y. Kvashnin, A. Hariki, H. Ikeno, H. Ramanantoanina, C. Daul, B. Delley, M. Odelius, M. Lundberg, O. Kuhn, S. I. Bokarev, E. Shirley, J. Vinson, K. Gilmore, M. Stener, G. Fronzoni, P. Declava, P. Kruger, M. Retegan, Y. Joly, C. Vorwerk, C. Draxl, J. Rehr, and A. Tanaka, "2p X-ray absorption spectroscopy of 3d transition metal systems," *Journal of Electron Spectroscopy and Related Phenomena* **249**, 147061 (2021).
- <sup>55</sup>I. Hernández and F. Rodríguez, "On the pressure-induced spin transition in  $\text{CoCl}_2$ : interplay between Jahn-Teller effect and spin state in  $\text{Co}^{2+}$ ," *Journal of Physics: Conference Series* **121**, 042006 (2008).
- <sup>56</sup>R. H. Potze, G. A. Sawatzky, and M. Abbate, "Possibility for an intermediate-spin ground state in the charge-transfer material  $\text{SrCoO}_3$ ," *Phys. Rev. B* **51**, 11501–11506 (1995).
- <sup>57</sup>M. Merz, P. Nagel, C. Pinta, A. Samartsev, H. v. Löhneysen, M. Wissinger, S. Uebe, A. Assmann, D. Fuchs, and S. Schuppler, "X-ray absorption and magnetic circular dichroism of  $\text{LaCoO}_3$ ,  $\text{La}_{0.7}\text{Ce}_{0.3}\text{CoO}_3$ , and  $\text{La}_{0.7}\text{Sr}_{0.3}\text{CoO}_3$  films: Evidence for cobalt-valence-dependent magnetism," *Phys. Rev. B* **82**, 174416 (2010).
- <sup>58</sup>C. Pinta, D. Fuchs, M. Merz, M. Wissinger, E. Arac, H. v. Löhneysen, A. Samartsev, P. Nagel, and S. Schuppler, "Suppression of spin-state transition in epitaxially strained  $\text{LaCoO}_3$ ," *Phys. Rev. B* **78**, 174402 (2008).
- <sup>59</sup>M. Abbate, J. C. Fuggle, A. Fujimori, L. H. Tjeng, C. T. Chen, R. Potze, G. A. Sawatzky, H. Eisaki, and S. Uchida, "Electronic structure and spin-state transition of  $\text{LaCoO}_3$ ," *Phys. Rev. B* **47**, 16124–16130 (1993).
- <sup>60</sup>A. S. Harvey, Z. Yang, A. Infortuna, D. Beckel, J. A. Purton, and L. J. Gauckler, "Development of electron holes across the temperature-induced semiconductor–metal transition in  $\text{Ba}_{1-x}\text{Sr}_x\text{Co}_{1-y}\text{Fe}_y\text{O}_{3-\delta}$  ( $x, y = 0.2 - 0.8$ ): a soft x-ray absorption spectroscopy study," *Journal of Physics: Condensed Matter* **21**, 015801 (2008).
- <sup>61</sup>X. Li, Y. Sun, F. Ren, Y. Bai, and Z. Cheng, "Smart oxygen vacancy engineering to enhance water oxidation efficiency by separating the different effects of bulk and surface vacancies," *Materials Today Energy* **19**, 100619 (2021).
- <sup>62</sup>M. Ghiasi, M. U. Delgado-Jaime, A. Malekzadeh, R.-P. Wang, P. S. Miedema, M. Beye, and F. M. F. de Groot, "Mn and Co Charge and Spin Evolutions in  $\text{LaMn}_{1-x}\text{Co}_x\text{O}_3$  Nanoparticles," *The Journal of Physical Chemistry C* **120**, 8167–8174 (2016).
- <sup>63</sup>M. M. van Schooneveld, R. Kurian, A. Juhin, K. Zhou, J. Schlappa, V. N. Strocov, T. Schmitt, and F. M. F. de Groot, "Electronic Structure of  $\text{CoO}$  Nanocrystals and a Single Crystal Probed by Resonant X-ray Emission Spectroscopy," *The Journal of Physical Chemistry C* **116**, 15218–15230 (2012).
- <sup>64</sup>F. M. F. de Groot, M. Grioni, J. C. Fuggle, J. Ghijsen, G. A. Sawatzky, and H. Petersen, "Oxygen 1s x-ray-absorption edges of transition-metal oxides," *Phys. Rev. B* **40**, 5715–5723 (1989).
- <sup>65</sup>J. Suntivich, W. T. Hong, Y.-L. Lee, J. M. Rondinelli, W. Yang, J. B. Goodenough, B. Dabrowski, J. W. Freeland, and Y. Shao-Horn, "Estimating Hybridization of Transition Metal and Oxygen States in Perovskites from O K-edge X-ray Absorption Spectroscopy," *The Journal of Physical Chemistry C* **118**, 1856–1863 (2014).
- <sup>66</sup>L. Wu, M. Chen, C. Li, J. Zhou, L. Shen, Y. Wang, Z. Zhong, M. Feng, Y. Zhang, K. Han, T. V. Venkatesan, S. J. Pennycook, P. Yu, J. Ma, X. R. Wang, and C.-W. Nan, "Ferromagnetism and matrix-dependent charge transfer in strained  $\text{LaMnO}_3$ – $\text{LaCoO}_3$  superlattices," *Materials Research Letters* **6**, 501–507 (2018).
- <sup>67</sup>A. V. A. Dogra, A. Gupta, and J. J. Pulikkotil, "Retentivity of spin state transitions in  $\text{LaCoO}_3$  with chemical disorder," *RSC Adv.* **6**, 1403–1407 (2016).
- <sup>68</sup>V. V. Mehta, N. Biskup, C. Jenkins, E. Arenholz, M. Varela, and Y. Suzuki, "Long-range ferromagnetic order in  $\text{LaCoO}_{3-\delta}$  epitaxial films due to the interplay of epitaxial strain and oxygen vacancy ordering," *Phys. Rev. B* **91**, 144418 (2015).
- <sup>69</sup>K. Tomiyasu, J. Okamoto, H. Y. Huang, Z. Y. Chen, E. P. Sinaga, W. B. Wu, Y. Y. Chu, A. Singh, R.-P. Wang, F. M. F. de Groot, A. Chainani, S. Ishihara, C. T. Chen, and D. J. Huang, "Coulomb Correlations Intertwined with Spin and Orbital Excitations in  $\text{LaCoO}_3$ ," *Phys. Rev. Lett.* **119**, 196402 (2017).
- <sup>70</sup>Z. Hu, H. Wu, M. W. Haverkort, H. H. Hsieh, H. J. Lin, T. Lorenz, J. Baier, A. Reichl, I. Bonn, C. Felser, A. Tanaka, C. T. Chen, and L. H. Tjeng, "Different Look at the Spin State of  $\text{Co}^{3+}$  Ions in a  $\text{CoO}_5$  Pyramidal Coordination," *Phys. Rev. Lett.* **92**, 207402 (2004).
- <sup>71</sup>F. de Groot, "X-ray absorption and dichroism of transition metals and their compounds," *Journal of Electron Spectroscopy and Related Phenomena* **67**, 529–622 (1994).
- <sup>72</sup>M. G. Herrera-Yáñez, J. A. Guerrero-Cruz, M. Ghiasi, H. Elnaggar, A. de la Torre-Rangel, L. A. Bernal-Guzmán, R. Flores-Moreno, F. M. F. de Groot, and M. U. Delgado-Jaime, "Fitting Multiplet Simulations to L-Edge XAS Spectra of Transition-Metal Complexes Using an Adaptive Grid Algorithm," *Inorganic Chemistry* **62**, 3738–3760 (2023).
- <sup>73</sup>S. K. Chaluvasi, V. Polewczyk, A. Y. Petrov, G. Vinai, L. Braglia, J. M. Diez, V. Pierron, P. Perna, L. Mechin, P. Torelli, and P. Orgiani, "Electronic Properties of Fully Strained  $\text{La}_{1-x}\text{Sr}_x\text{MnO}_3$  Thin Films Grown by Molecular Beam Epitaxy ( $0.15 \leq x \leq 0.45$ )," *ACS Omega* **7**, 14571–14578 (2022).
- <sup>74</sup>G. Radtke, C. Maunders, S. Lazar, F. de Groot, J. Etheridge, and G. Botton, "The role of Mn in the electronic structure of  $\text{Ba}_3\text{Ti}_2\text{MnO}_9$ ," *Journal of Solid State Chemistry* **178**, 3426–3430 (2005).
- <sup>75</sup>B. Gilbert, B. H. Frazer, A. Belz, P. G. Conrad, K. H. Nealson, D. Haskel, J. C. Lang, G. Srajer, and G. De Stasio, "Multiple Scattering Calculations of Bonding and X-ray Absorption Spectroscopy of Manganese Oxides," *The Journal of Physical Chemistry A* **107**, 2839–2847 (2003).
- <sup>76</sup>N. Gauquelin, E. Benckiser, M. K. Kinyanjui, M. Wu, Y. Lu, G. Christiani, G. Logvenov, H.-U. Habermeier, U. Kaiser, B. Keimer, and G. A. Botton, "Atomically resolved EELS mapping of the interfacial structure of epitaxially strained  $\text{LaNiO}_3/\text{LaAlO}_3$  superlattices," *Phys. Rev. B* **90**, 195140 (2014).



## SUPPLEMENTAL MATERIAL

### S1: Pulsed laser deposition parameters

TABLE S1. PLD growth parameters for the different layers. The substrate-target distance was 50 mm and the spot size of the ablated area was 1.8 mm<sup>2</sup> for all layers.

	Fluence (J/cm <sup>2</sup> )	Temperature (°C)	$pO_2$ (mbar)	Repetition rate (Hz)
LaNiO <sub>3</sub>	1.8	450	0.04	2
LaCoO <sub>3</sub>	1.8	670	0.1	2
LaMnO <sub>3</sub>	1.8	670	0.1	1
LaTiO <sub>3</sub>	1.8	670	$2 \cdot 10^{-3}$	1
LaAlO <sub>3</sub>	1.3	670	$2 \cdot 10^{-3}$	1

### S2: Charge transfer multiplet calculations parameters

The semi-empirical simulation parameters for Co<sup>2+</sup> HS, Co<sup>3+</sup> LS, Co<sup>3+</sup> HS and Co<sup>4+</sup> HS are similar to the parameters reported in literature<sup>28,62,69</sup>. The crystal field splitting,  $10D_q$ , for Co<sup>3+</sup> LS and HS were optimized to match experimental spectra of EuCoO<sub>3</sub> and Sr<sub>2</sub>CoO<sub>3</sub>Cl<sup>70</sup>. The  $10D_q$  value of Co<sup>2+</sup> HS was optimized match the distance between first three peaks of the Co<sup>2+</sup> feature in the L<sub>3</sub> edges presented in this work. The parameters for Co<sup>4+</sup> were optimized to match the experimental spectrum of SrCoO<sub>3</sub><sup>61</sup>. As the calculations do not give absolute energy positions, the spectra are shifted in energy using the experimental spectra listed above.

TABLE S2. Parameters used for charge transfer multiplet calculations of Co L<sub>2,3</sub> edges. The total crystal field is a combination of the ionic value  $10D_q$  (ionic) and a covalent contribution that is approximately 0.3 for all cases. The  $10D_q$  is reduced by  $\sim 20\%$  in the final state with respect to the ground state.

	Crystal field		Slater reduction			$\Delta$	Charge transfer			
	Symmetry	$10D_q$ (ionic)	$F_{dd}$	$F_{pd}$	$G_{pd}$		$U_{dd}$	$U_{pd}$	$T_{eg}$	$T_{t2g}$
Co <sup>2+</sup> HS	O <sub>h</sub>	0.85	0.9	0.9	0.9	3.0	6.5	7.5	2	1
Co <sup>3+</sup> LS	O <sub>h</sub>	1.3	0.8	0.8	0.8	1.5	6.5	7.5	2	1
Co <sup>3+</sup> HS	O <sub>h</sub>	0.8	0.8	0.8	0.8	1.5	6.5	7.5	2	1
Co <sup>4+</sup> HS	O <sub>h</sub>	1.6	0.8	0.8	0.8	-1.5	6.5	7.5	2	1

For Mn<sup>2+</sup>, parameters similar to reference 71 are chosen. The symmetry of Mn<sup>3+</sup> is chosen to be D<sub>4h</sub> rather than O<sub>h</sub> as Jahn-Teller distortions tend to result in a small tetragonal distortion in the crystal field<sup>72,73</sup>. To model the high covalency of Mn<sup>4+</sup>, the Slater integrals were reduced further from their atomic values<sup>74</sup>. The simulation parameters chosen for Mn<sup>3+</sup> and Mn<sup>4+</sup> are similar to the parameters chosen in references 73 and 62. The relative energy positions of each valence state are shifted to match reference spectra of MnO, Mn<sub>2</sub>O<sub>3</sub> and MnO<sub>2</sub><sup>75</sup>.

TABLE S3. Parameters used for charge transfer multiplet calculations of Mn L<sub>2,3</sub> edges. The total crystal field is a combination of the ionic value  $10D_q$  (ionic) and a covalent contribution that is approximately 0.3 for all cases. The  $10D_q$  is reduced by  $\sim 20\%$  in the final state with respect to the ground state.

	Crystal field		Slater reduction			$\Delta$	Charge transfer			
	Symmetry	$10D_q$ (ionic)	$F_{dd}$	$F_{pd}$	$G_{pd}$		$U_{dd}$	$U_{pd}$	$T_{eg}$	$T_{t2g}$
Mn <sup>2+</sup>	O <sub>h</sub>	0.8	0.9	0.9	0.9	-	-	-	-	-
Mn <sup>3+</sup>	D <sub>4h</sub> <sup>a</sup>	1.55	0.8	0.8	0.8	4	6.5	7.5	2	1
Mn <sup>4+</sup>	O <sub>h</sub>	2.1	0.4	0.5	0.5	1	6.5	7.5	2	1

<sup>a</sup> D<sub>t</sub>=-0.02, D<sub>s</sub> = 0.1

## S3: Thin film characterization

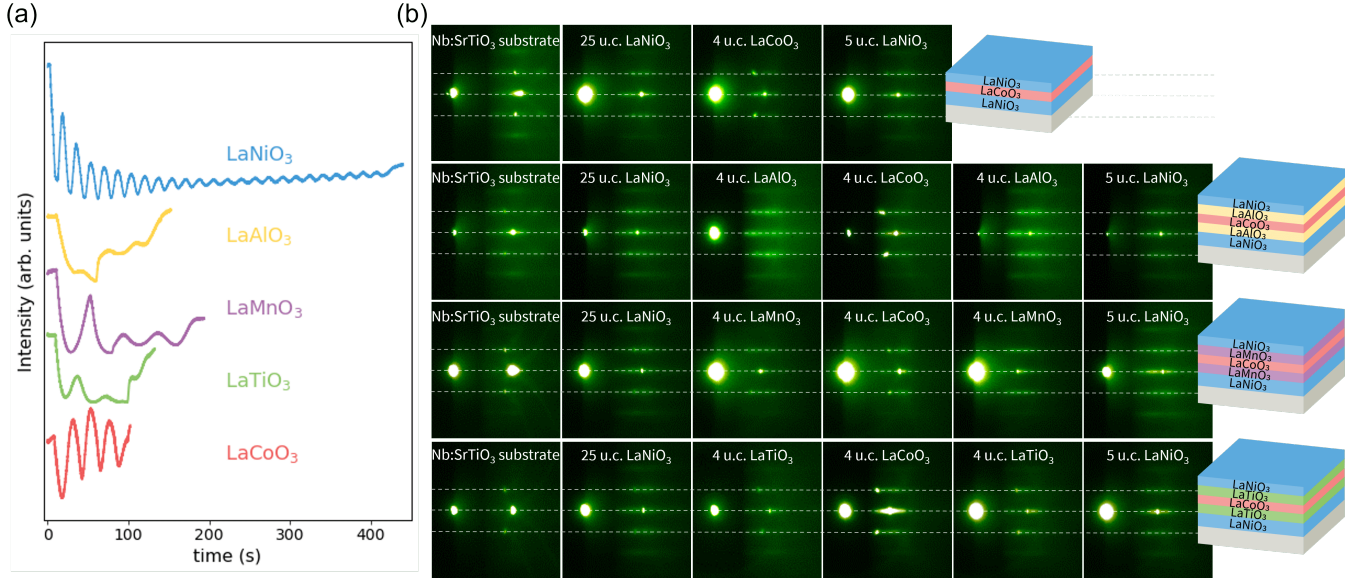


FIG. S1. a) Integrated intensity of the specular spot as a function of time during the deposition of each layer. Sharp increases are due to a manual increase of the filament current. b) RHEED patterns after the deposition of each layer.

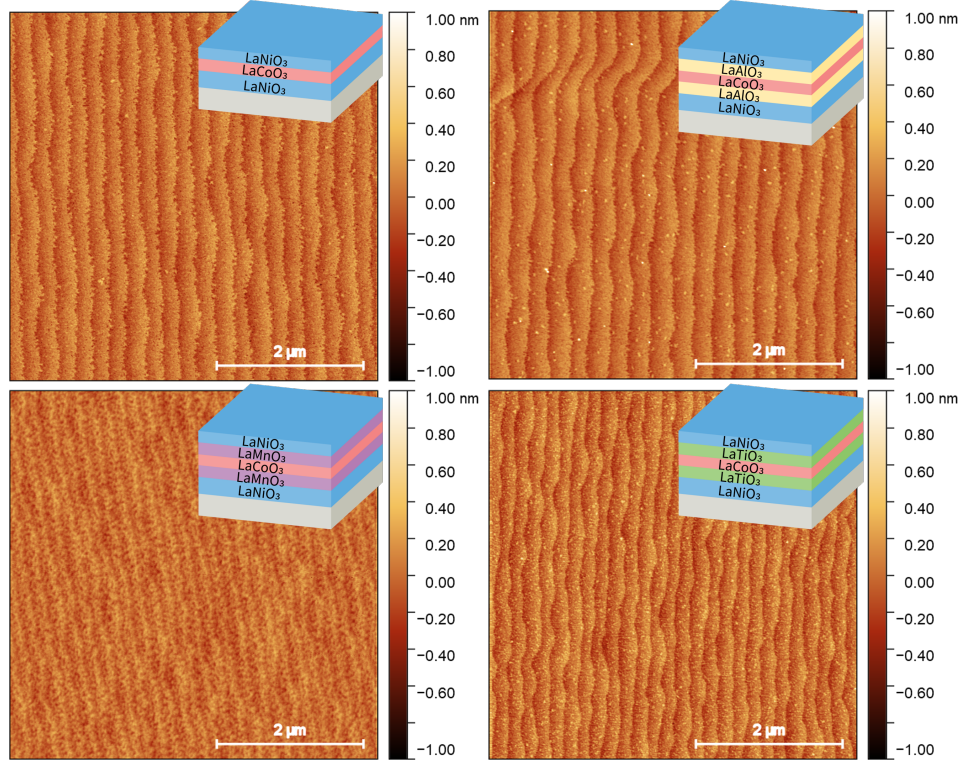


FIG. S2. AFM images of the LaCoO<sub>3</sub> multilayers with the (a) LaNiO<sub>3</sub>-LaCoO<sub>3</sub> interface, (b) LaAlO<sub>3</sub>-LaCoO<sub>3</sub> interface, (c) LaMnO<sub>3</sub>-LaCoO<sub>3</sub> interface, (d) LaTiO<sub>3</sub>-LaCoO<sub>3</sub> interface.

## S4: Additional XAS data and fitting

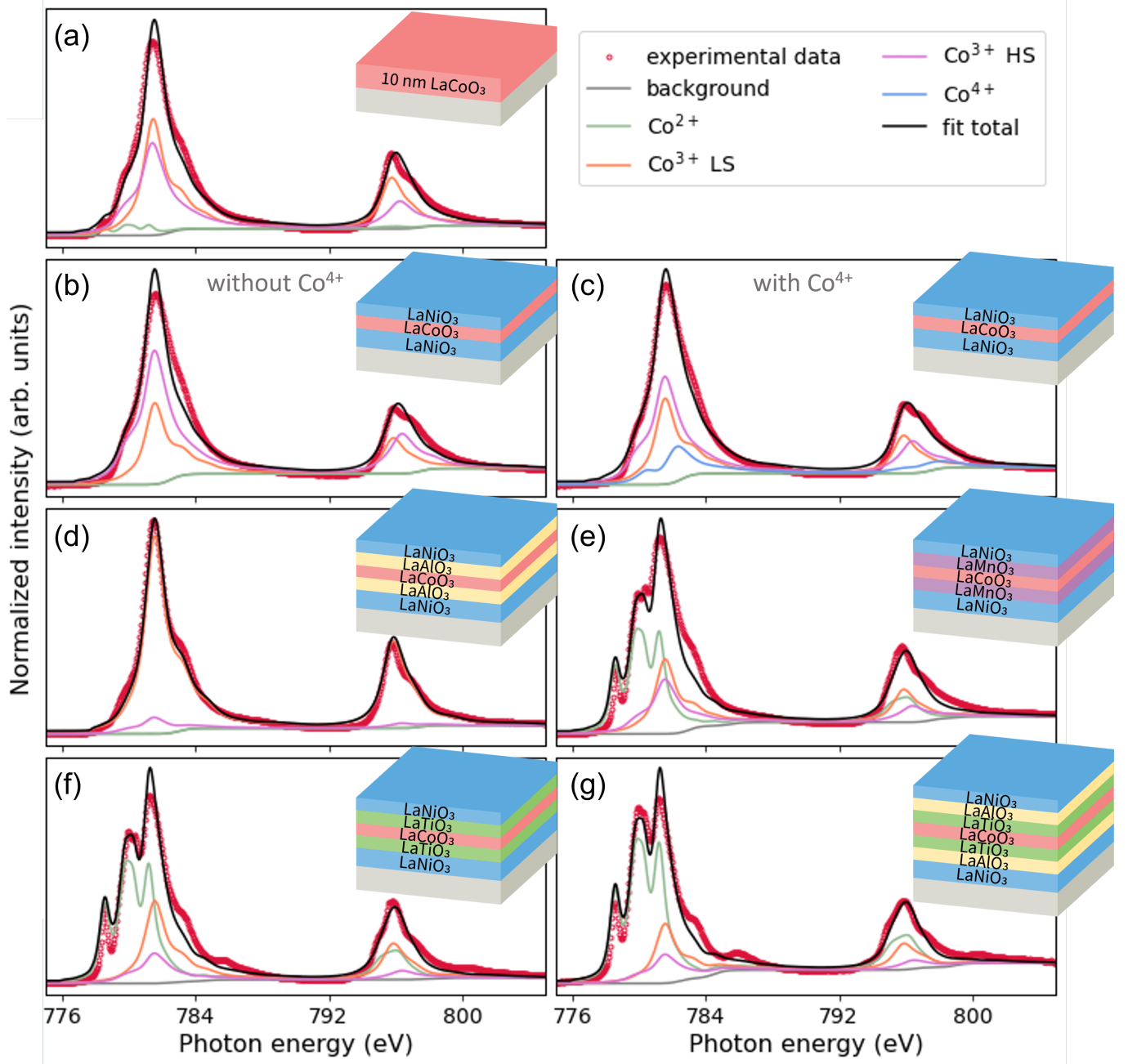


FIG. S3. Linear combination fits of calculated spectra for different Co valence states.

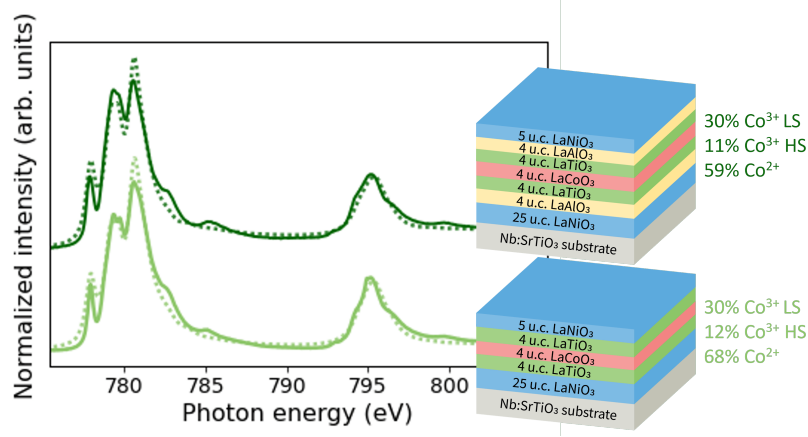


FIG. S4. Co  $L_{2,3}$  edges with and without a LaAlO<sub>3</sub> spacer between LaTiO<sub>3</sub> and LaNiO<sub>3</sub> (solid lines). The dotted lines represent a linear combination fit of simulated spectra using CTM calculations. Numbers on the right side indicate relative contributions of simulated spectra to fit.

#### Mn $L$ edges of the LaCoO<sub>3</sub>-LaMnO<sub>3</sub> interface

XAS spectra of the sample with the LaCoO<sub>3</sub>-LaMnO<sub>3</sub> interface and a single LaMnO<sub>3</sub> layer are shown in figure S5. Furthermore, a multilayer with a single LaMnO<sub>3</sub> layer in between two LaCoO<sub>3</sub> layers is included. Both samples with a LaCoO<sub>3</sub>-LaMnO<sub>3</sub> interfaces show a shift in photon energy, implying a higher oxidation state compared to a single LaMnO<sub>3</sub> layer. Comparison of the experimental spectra with calculated spectra of Mn<sup>2+</sup>, Mn<sup>3+</sup> and Mn<sup>4+</sup> are shown in figure S5b to help identify the differences between experimental spectra. As Mn  $L$  edges are highly affected by Jahn-Teller distortions and covalency effects<sup>72</sup>, we refrain from fitting the calculations to the experimental spectra. However, the shift in photon energy and the change in spectral shape indicate a higher Mn<sup>4+</sup> contribution for the multilayers compared to the single layer. Interestingly, a layer of LaMnO<sub>3</sub> between two LaCoO<sub>3</sub> layers results in a higher Mn<sup>4+</sup> contribution than the sample with LaCoO<sub>3</sub> between two LaMnO<sub>3</sub> layers, pointing towards more charge transfer between Mn and Co compared to Ni and Co.

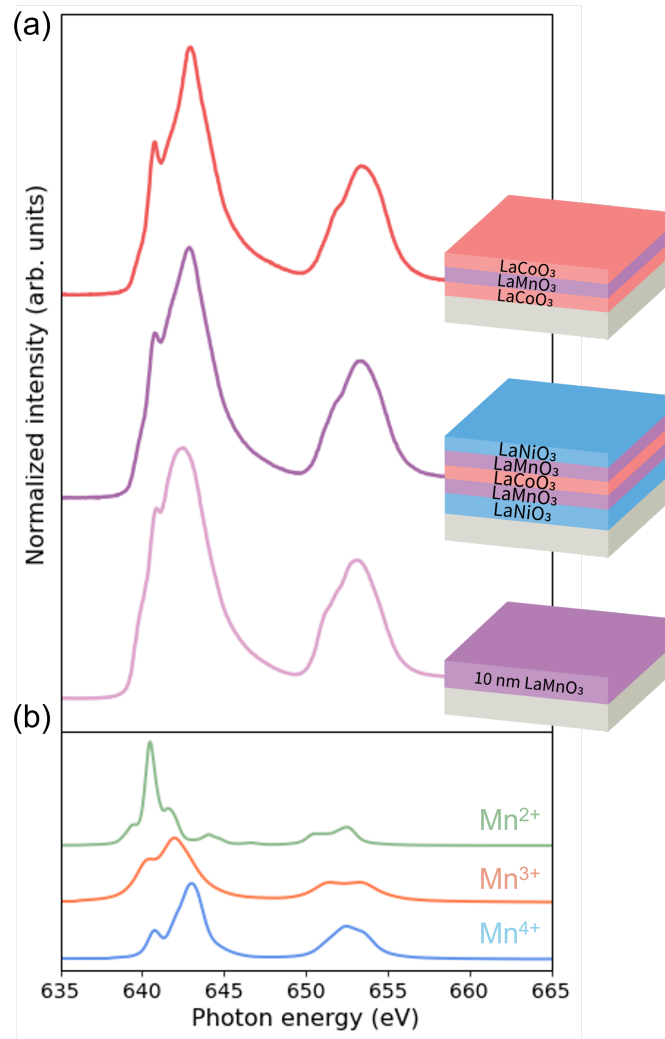


FIG. S5. (a) Mn L<sub>2,3</sub> edges of multilayers with LaCoO<sub>3</sub>-LaMnO<sub>3</sub> interfaces as well as a single LaMnO<sub>3</sub> layer. (b) CTM calculations of Mn<sup>2+</sup>, Mn<sup>3+</sup> and Mn<sup>4+</sup> valence states.



## S5: EELS data

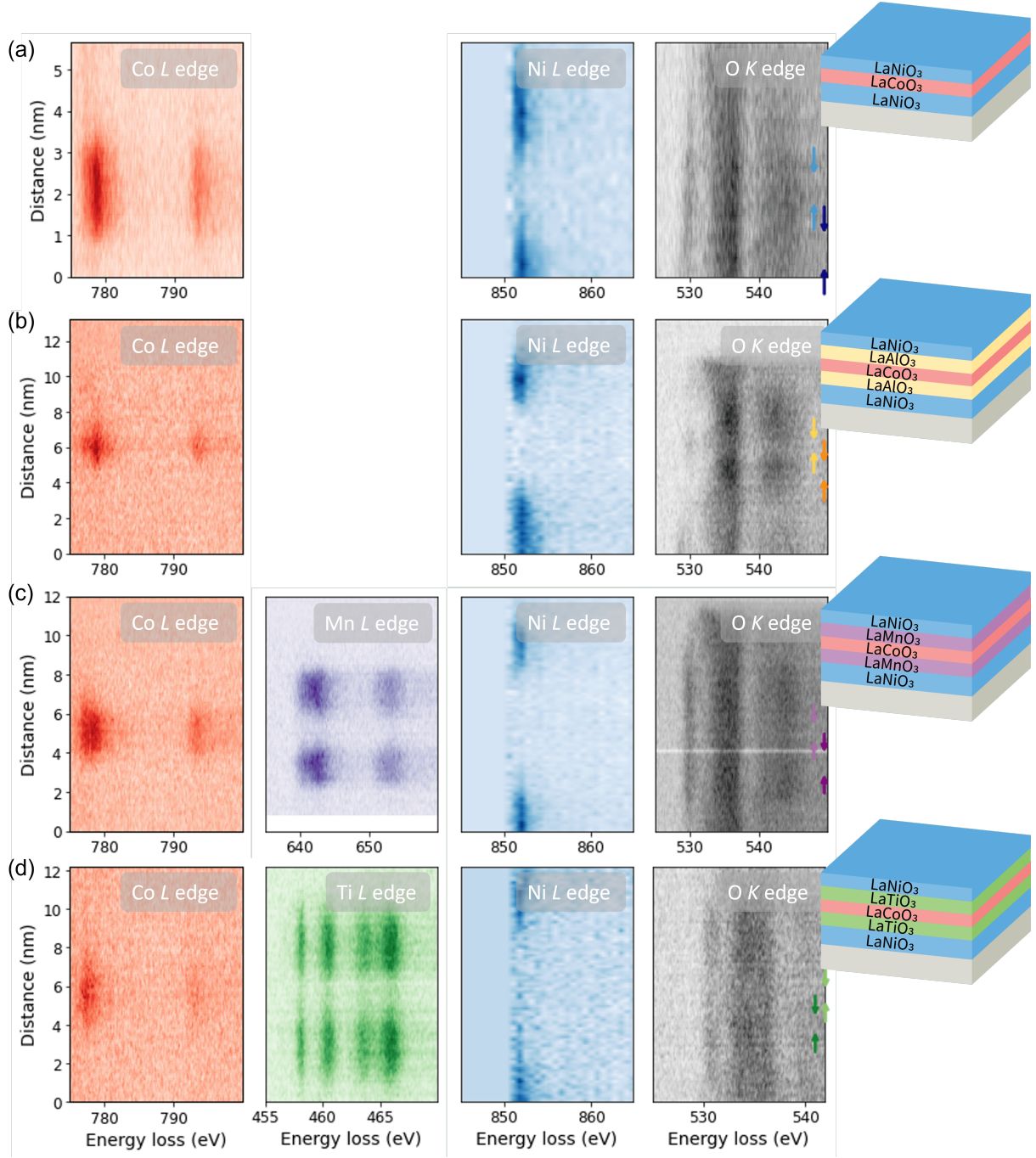


FIG. S6. EELS of the TM *L* edges and O *K* edges in the multilayers containing the (a) LaNiO<sub>3</sub>-LaCoO<sub>3</sub> interface, (b) LaAlO<sub>3</sub>-LaCoO<sub>3</sub> interface, (c) LaMnO<sub>3</sub>-LaCoO<sub>3</sub> interface, (d) LaTiO<sub>3</sub>-LaCoO<sub>3</sub> interface. The Mn *L* edge in (c) is taken at a different but equivalent position. The data is shifted over the spatial axis such that the Co and Ni signals match the between the two positions. The arrows indicate integration regions for the spectra in figure S7 and S8.

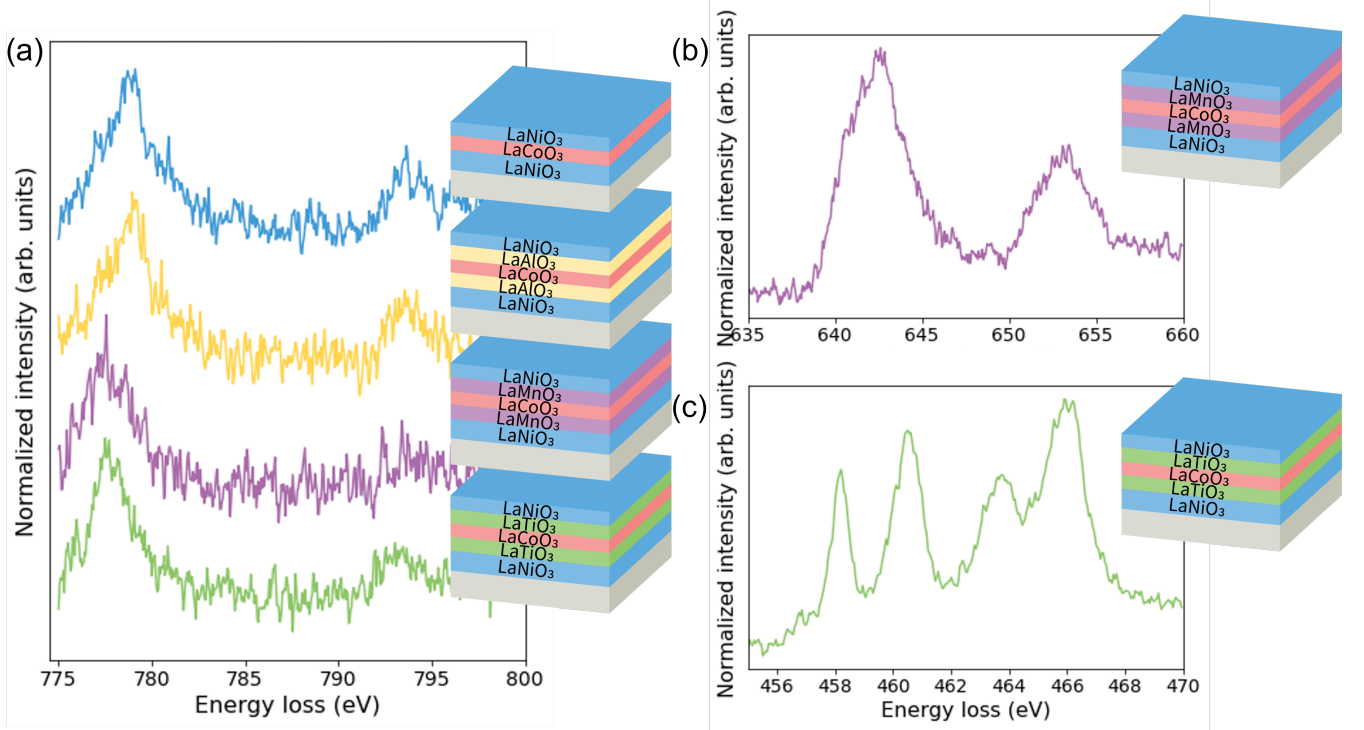


FIG. S7. (a) EELS traces of the Co  $L$  edges for the different multilayers extracted from the EELS maps by integrating for the full  $\text{LaCoO}_3$  layer. (b) Mn  $L$  edge for the  $\text{LaMnO}_3$ - $\text{LaCoO}_3$  multilayer integrated for the bottom  $\text{LaMnO}_3$  layer. (c) Ti  $L$  edge  $\text{LaTiO}_3$ - $\text{LaCoO}_3$  multilayer integrated for the bottom  $\text{LaTiO}_3$  layer.

### O K edges

Figure S8 shows the O K edges extracted at the center of the  $\text{LaCoO}_3$  layer (solid lines) and the layer below (dotted lines) for each of the multilayers. The corresponding integrated regions in the EELS maps are indicated by the colored arrows in figure S6. We find that the pre-edge at  $\sim 530$  eV is very low in intensity for the sample with the  $\text{LaAlO}_3$ - $\text{LaCoO}_3$  interface. The pre-edge is related to electron excitations from the O  $1s$  state to the hybridized O  $2p$ -TM  $3d$  state and therefore provides information about the hybridized TM  $3d$  states<sup>64,65</sup>. Due to the empty  $d$  orbitals of  $\text{LaAlO}_3$ , no significant hybridization and therefore no pre-edge feature is expected in these layers. However, this electronic state seems to extend into the  $\text{LaCoO}_3$  layer. Furthermore, the pre-edge position is very similar inside the  $\text{LaCoO}_3$  layer compared to the layer below for the samples with the  $\text{LaMnO}_3$ - $\text{LaCoO}_3$  and  $\text{LaTiO}_3$ - $\text{LaCoO}_3$  as well. Taken together, these observations suggest that the signal of the O K edges is more delocalized than the signal from the cations and exceeds the energy loss delocalization of approximately  $4 \text{ \AA}$ . A similar effect was previously observed for  $\text{LaNiO}_3$ - $\text{LaAlO}_3$  superlattices<sup>76</sup>. We hypothesize that the delocalization of the electronic states of oxygen is more prominent compared to the cations due to the hybridized nature of the O  $2p$  states. Therefore, we use TM edges for charge transfer evaluation, which cannot be resolved with the more delocalized O K edges.

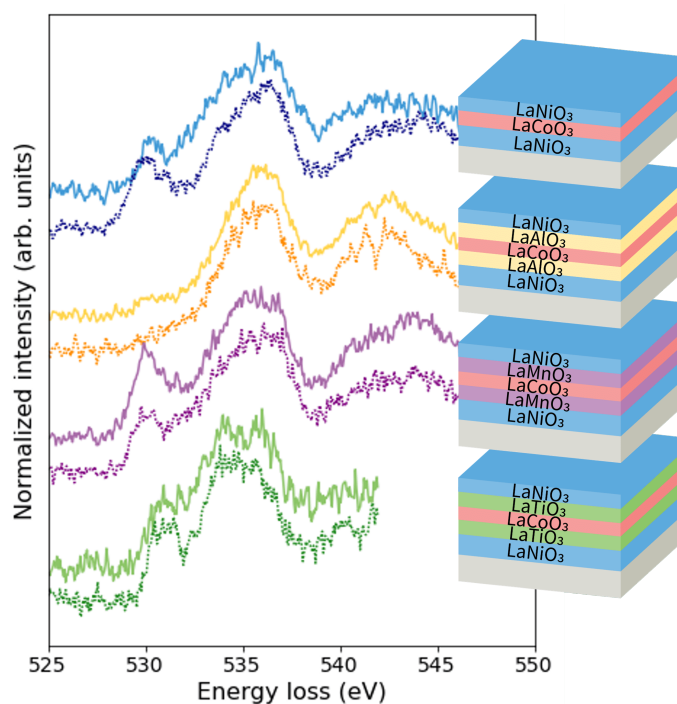


FIG. S8. EELS traces of the O K edges for the different multilayers extracted from the EELS maps in the center of the  $\text{LaCoO}_3$  layer (solid lines) and layer below (dotted lines) as indicated by the colored arrows in figure S6.